The Cosmic Muon Flux in the ATLAS Detector at the Large Hadron Collider

by

Ewan Chin Hill
B.Sc., University of Waterloo, 2008

A Thesis Submitted in Partial Fulfillment of the
Requirements for the Degree of

MASTER OF SCIENCE

in the Department of Physics and Astronomy

The Cosmic Muon Flux in the ATLAS Detector at the Large Hadron Collider

by

Ewan Chin Hill
B.Sc., University of Waterloo, 2008

Supervisory Committee

Dr. Isabel Trigger, Co-Supervisor
(Department of Physics and Astronomy & TRIUMF)

Dr. Michel Lefebvre, Co-Supervisor
(Department of Physics and Astronomy)

Supervisory Committee

Dr. Isabel Trigger, Co-Supervisor
(Department of Physics and Astronomy & TRIUMF)

Dr. Michel Lefebvre, Co-Supervisor
(Department of Physics and Astronomy)

ABSTRACT

Many ATLAS analyses study events with muons in them including those searching for the Higgs boson and new physics. Cosmics muons, however, can also occasionally enter the detector and mimic the trajectory of a muon from one of the collisions produced by CERN's Large Hadron Collider. By understanding the different ways ATLAS triggers on, collects, reconstructs, and analyses data from cosmic rays and collisions, the flux of cosmic muons with transverse momenta above 20 GeV in the central region of the detector was measured to be $1.34 \pm 0.06\,(\text{stat.})$ s^{-1} m^{-2}. At the same time the cosmic muon charge ratio has been measured to be $1.3 \pm 0.1\,(\text{stat.})$. This measurement of the cosmic muon flux in ATLAS is the first step in quantifying the sizes of the cosmic muon backgrounds to various physics analyses that look for events with muons.

Contents

List of Tables

List of Figures

ACKNOWLEDGEMENTS

Many thanks go to my supervisor Dr. Isabel Trigger for her constant support throughout the entire project. She taught me a great deal and it is always a pleasure to work with her. I would also like to thank Dominique Fortin for helping set up the analysis and answering my questions. Everyone from the UVic and TRIUMF ATLAS groups provided me great assistance and it is much appreciated. My thanks also go out to Michel Lefebvre and to rest of the faculty and staff of the UVic Physics and Astronomy department. Much valued support was also provided by: Frank Berghaus, Tayfun Ince, Xander Baker, Greg King, André Gaudin, Jordan Myslik, Matthias Le Dall, and Patrick deNiverville. I would also like to thank my parents, my brother, and my aunt Edith Chin for their help in my education over the years.

I have had a very enjoyable time at UVic and much of that I owe to my friends in physics, chemistry, the grad house, and to the Chafrican Feeling Tasters. There are a number of people who helped me get to where I am today and I greatly appreciate their friendship: Pam Lee, Adam Jones-Delcorde, Rachel Newman, Sorina Truica, Jimmie Clarke, Brad Moores, Jenny Nguyen, Bert Ji, Jane Robinson, Robbie Henderson, Sheena Alexander, my other UW physics friends, and the Pau House.

DEDICATION

To my parents, Ian and Elizabeth,
my brother, Bryce,
and the rest of the Flying Circus aboard Red Dwarf.

To Pam, a friend for the ages.

Chapter 1

Introduction

Particle physics is the study of subatomic particles and their interactions. The Standard Model is the physics theory that particle physicists have found to give the most accurate and complete description of the subject thus far. Many parts of the Standard Model have been thoroughly studied over the last few decades but an essential ingredient of the theory, the Higgs boson, has yet to be found in an experiment.

CERN's[1] LHC[2] is a particle accelerator that will help test the Standard Model and perhaps find new physics beyond the Standard Model. This synchrotron accelerates protons up to a nominal energy of 7 TeV per beam and collides them. Located on the border between Switzerland and France in the Rhone Valley near Geneva it is the world's highest energy particle accelerator since it collided beams for the first time at 1.18 TeV per beam on 8 December 2009. By circulating particles around its 27 km circumference and focusing the bunches of protons down to extremely small cross-sectional areas the accelerator can obtain very high luminosities and produce a large number of collisions in a short period of time. The processes that particle physicists want to study are rare and the collision rate is so high that only a small fraction of all the events can be recorded. To cope with this, the detectors along the LHC ring use triggering systems to automatically filter the collision data as it is being taken.

ATLAS, one of the two general-purpose detectors at the LHC was constructed to accomplish many goals, the main one being to find the Higgs boson. The Higgs mechanism in the Standard Model generates the masses of all the particles through electroweak symmetry breaking and predicts the existence of the Higgs boson. The

[1] The European Organization for Nuclear Research.
[2] Large Hadron Collider.

Higgs boson is the last particle predicted by the Standard Model still to be discovered. Depending on its mass it may decay into several different particles. The decays of the Higgs boson into two or four muons[3], if allowed, are among the channels in which the Higgs boson could be most quickly found. Muons are also seen in the decay of several other particles like the W and Z bosons and some particles in supersymmetry, a theory predicting new physics beyond the Standard Model. In general, the observation of a muon from an interaction is a good sign that a collision has produced new particles that were not present in the initial state. Looking for muons in events is one way in which the ATLAS triggering system and many physics analyses select events.

The collisions of the LHC beams are not the only source of muons in ATLAS. Cosmics rays that hit the Earth's atmosphere can produce muons that will travel to the Earth's surface. The flux of cosmic muons hitting the Earth's surface is approximately constant in time. As seen in Figure 1.1 some of the cosmic muons can enter the detector. Occasionally one of those cosmic muons will mimic the trajectory of a muon from a proton beam collision and will be difficult to distinguish from a muon from a collision event. Cosmic events where this happens would be a background to other physics studies that look for events with muons. Currently ATLAS uses a parameter inversion technique (see section 6.5) to estimate the cosmic muon background but this method is not always ideal.

The purpose of this thesis is to measure the flux of high-momentum cosmic muons through the central region of the detector with the aim of helping to quantify the size of the cosmic muon background in physics analyses. Chapter 2 describes the ATLAS detector, while Chapter 3 describes the timing and triggering and Chapter 4 the methods of reconstructing the data. Chapter 5 gives an overview of muon physics both for muons coming from cosmic rays and muons coming from collisions.
Chapters 6 and 7 discuss the procedure and results of the cosmic muon flux analysis respectively and the conclusions are given in Chapter 8.

[3]In this thesis the term "muon" is used to describe both positive and negatively charged muons unless specified otherwise.

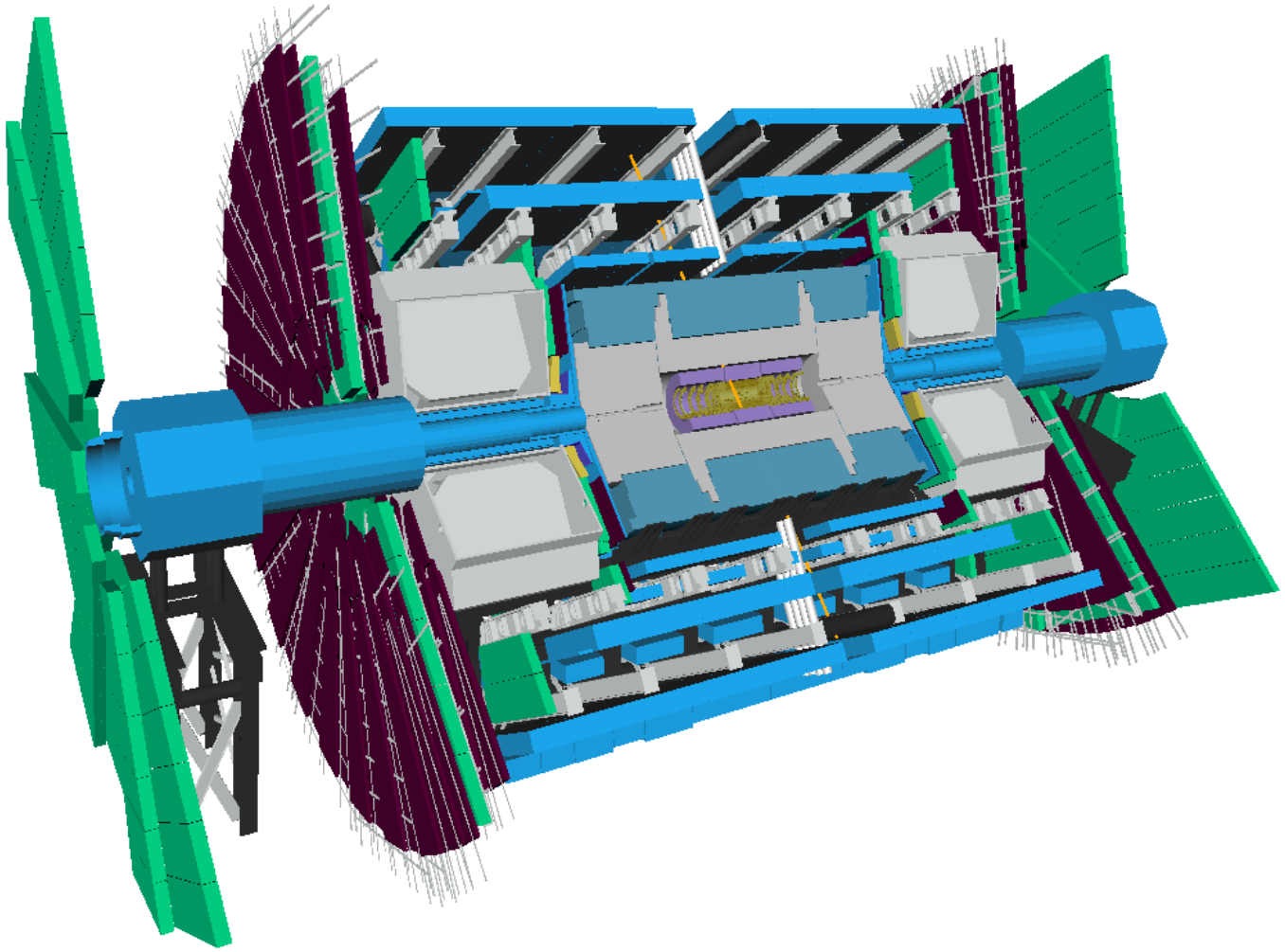

Figure 1.1: Track of a cosmic muon (in orange) that passed all the cuts in the ATLAS detector (run 152344, LB 211, event 951570).

Chapter 2

The ATLAS Detector

ATLAS is a multipurpose experiment built at CERN's LHC to study the fundamental particles of nature and their interactions at the smallest scales. Producing the rare interactions that the ATLAS collaboration wants to study requires extremely high energies and the Large Hadron Collider is the world's highest energy particle accelerator. It was built in the pre-existing tunnel that once housed the Large Electron Positron collider (LEP). The LHC is the same radius as LEP; however, it can accelerate two proton beams, instead of an electron beam and a positron beam, and collides them at much higher energies. The LHC has a nominal energy of 7 TeV per beam and in 2010/2011 the energy was 3.5 TeV per beam. By accelerating bunches of protons in circles it can take them up to high energies and when colliding particles at high enough energies, new particles can be produced that are different from those collided. The new particles or their decay products can be detected by ATLAS.

ATLAS is located in a cavern almost 100 m underground and is approximately 44 m long and 25 m in diameter as shown in Figure 2.1. The detector includes a cylindrical region around the beam called the "barrel" and disk-like "end-caps" on each end. In the ATLAS coordinate system both the x and y axes are in the plane orthogonal to the beam pipe with the x-axis pointing towards the centre of the LHC ring and the y-axis pointing upwards. The z-axis points along the LHC beam pipe and the coordinate system is centred on the centre of the detector. The radius (in cylindrical coordinates) is $R = \sqrt{x^2 + y^2}$. The angle ϕ is the azimuthal angle measured from the x-axis and θ is the polar angle measured from the z-axis. In practice $\eta = -\ln\left(\tan\left(\frac{\theta}{2}\right)\right)$ is used instead of θ where η is called the pseudorapidity, and is commonly used in hadron collider physics because the particle production is roughly

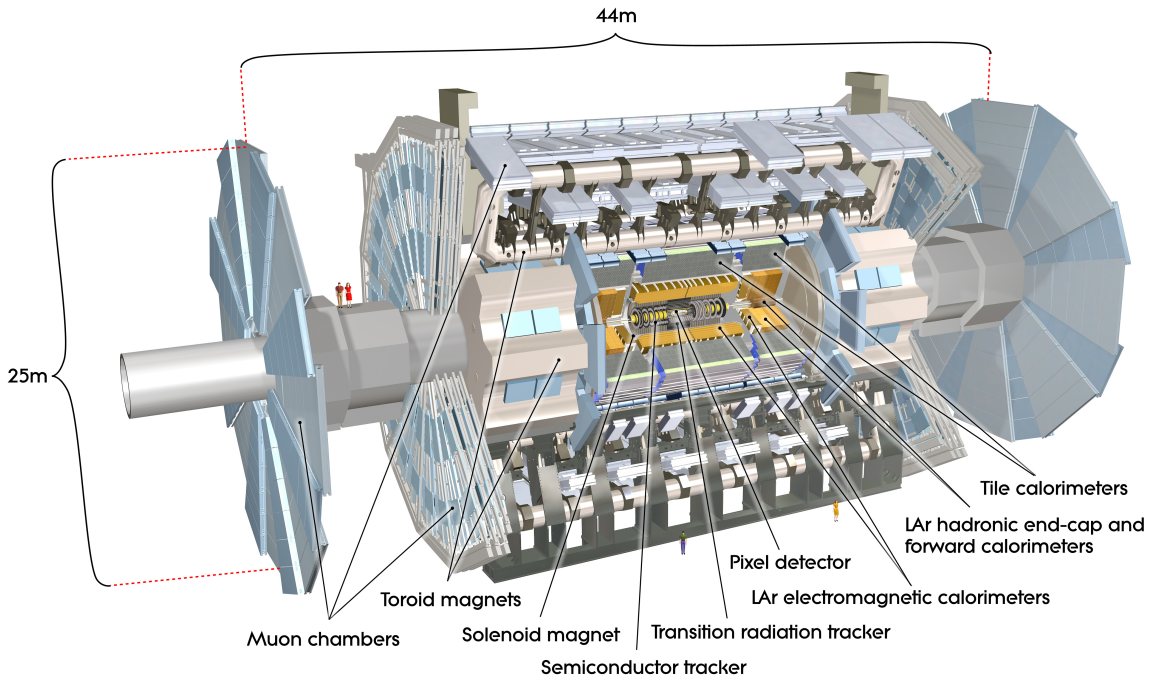

Figure 2.1: Cutaway diagram of ATLAS showing the major components of the detector [1].

constant as a function of η [2]. In hadron collider physics a particle's momentum[1] and energy are often studied in the transverse plane, where they are referred to as the transverse momentum, p_{T}, and transverse energy, E_{T}. These properties are often studied in the transverse plane because while the two colliding beams have the same energy, the partons within each of the colliding beam's protons do not carry equal shares of the momentum. As a result of this, the colliding partons' momenta in the $\pm z$ direction before the collision are unknown. However, the colliding partons have approximately zero momentum in the transverse direction and so the transverse momenta of all final-state particles must also sum to zero.

The ATLAS detector is built in roughly cylindrical layers, each designed to identify and measure different types of charged and neutral particles. The inner detector is the closest to the beam pipe and is used to make high-precision measurements of the particles' tracks as they travel outwards from the collision point. Surrounding the inner detector are the two calorimeters that are used to measure the energies of the particles. The innermost calorimeter is the electromagnetic calorimeter. It measures

[1]In this thesis natural units with $\hbar = c = 1$ are used so that momentum is given in GeV.

the energies of particles that lose most of their energy through electromagnetic interactions. Surrounding the electromagnetic calorimeter is the hadronic calorimeter. It is designed to accurately measure the energies of the particles produced at the collision that interact via the strong force. Surrounding the calorimeters is the muon spectrometer. Muons are the only known charged particles able to traverse the whole detector without decaying or losing a large fraction of their energy, so the muon spectrometer is the outermost layer of ATLAS. It is designed to perform accurate charged particle tracking. The last major component of ATLAS is the magnet system. The purpose of the magnets is to curve the trajectories of charged particles to determine their charges and momenta.

2.1 Inner Detector

The inner detector is the tracker used to measure the momenta and trajectories of all the charged particles. Its profile is approximately cylindrical and it is immersed in a 2 T axial magnetic field generated by a solenoid [1]. The detector was designed to be able to cope with a high rate of up to 1000 particles (from the collision point) passing through its acceptance region of $|\eta| < 2.5$ every 25 ns. The detector also requires high momentum and vertex resolution. To achieve these the inner detector of ATLAS has a fine detector granularity that is achieved by using silicon pixel or strip detectors close to the beam pipe. These silicon detectors make up the Pixel detector and the SemiConductor Tracker (SCT). Farther away from the beam pipe straw tubes make up the Transition Radiation Tracker (TRT).

2.1.1 Pixel and SCT

The precision tracking detectors (pixel and SCT) are arranged in concentric cylinders in the barrel region and in disks in the end-caps region as shown in Figure 2.2. They are made up of silicon detectors that cover the inner detector's full η range of $|\eta| < 2.5$. As is shown in Figure 2.3 the sensitive barrel region covers $50.5 < R < 122.5$ mm and $0 < |z| < 400.5$ mm for the pixel detector and $299 < R < 514$ mm and $0 < |z| < 749$ mm for the SCT. When a charged particle passes through one of these semiconductor detectors, a small ionization current is produced and detected.

Within the barrel, these are arranged into 3 pixel layers and 4 SCT layers. In the end-caps region they are arranged into 3 pixel disks and 9 SCT disks. The high

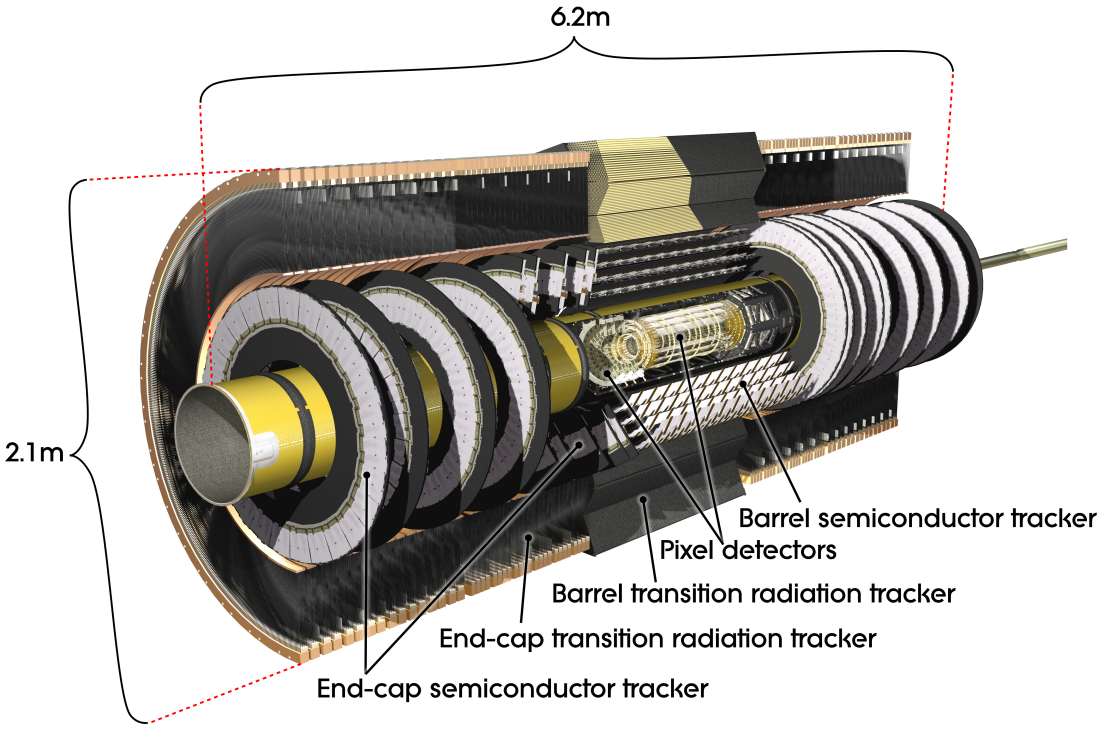

Figure 2.2: Cutaway diagram of ATLAS inner detector showing its major components [1].

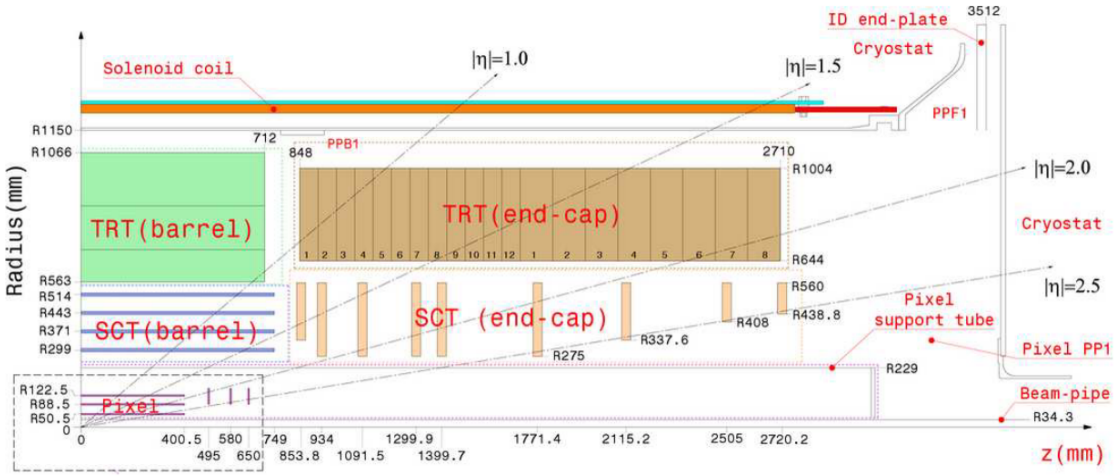

Figure 2.3: Plot of the ATLAS inner detector showing its dimensions [1].

precision tracking is achieved using discrete space-points from the pixel layers. The high precision tracking from the SCTs in both the barrel and the end-cap regions is achieved using two planes of silicon microstrip sensors placed back-to-back in each

layer. The two planes of sensors are parallel but the SCT strips are at an angle of 40 mrad from each other. This stereo angle allows the SCTs to measure the z coordinate in the barrel and the R coordinate in the end-cap region. In normal conditions these layers operate at $-5\,^{\circ}\mathrm{C}$ to $-10\,^{\circ}\mathrm{C}$. For a typical track in the barrel region, there will be 3 pixel hits and 8 SCT hits.

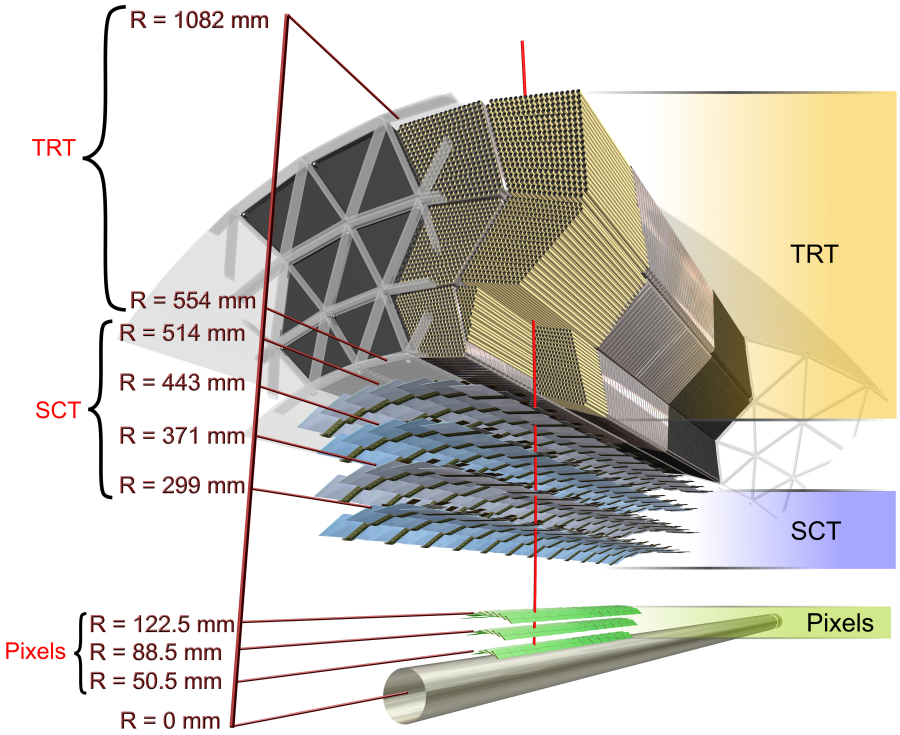

Figure 2.4: Cutaway diagram of ATLAS inner detector showing the trajectory of a charged track through the barrel [1].

2.1.2 Transition Radiation Tracker

Unlike the pixel and SCT, the TRT only covers the region of $|\eta| < 2.0$. The TRT straw tubes are small diameter drift tubes that are aligned parallel to the beam axis in the barrel region and radially in wheels in the end-caps region. On the walls of the tube there is a cathode and along the axis of the tube is an anode wire. The

tube contains a gas mixture which ionizes when a charged particle passes through the detector and the resulting charges are collected on the anode and cathode and a signal is detected. Within the barrel the straw tubes are arranged into 73 layers and in the end-caps they are arranged into 20 wheels. In normal conditions the TRT operates at room temperature. For a typical track in the barrel region, as can be seen in Figure 2.4, there are 36 hits. The drift tubes provide track measurements of $R - \phi$ in the barrel and z in the end-cap regions. The transition radiation from the traversing particles is used for particle identification.

2.2 Calorimeters

The ATLAS detector's calorimeters are used to measure the energy of the particles produced in collisions. The calorimeters have excellent electromagnetic (EM) calorimetry for measurements of electrons and photons, and very large coverage for the hadronic calorimetry for accurate jet reconstruction and missing energy measurements [1]. They are designed to ensure that particle showers are contained to limit leakage into the muon spectrometer.

The calorimeters cover the η range of $|\eta| < 4.9$ and to maximize containment there are approximately 9.7 interaction lengths (λ) of active calorimeter in the barrel region and approximately 10 interaction lengths of active calorimeter in the end-caps. In the η region of the EM calorimeter that matches the inner detector's coverage there is a fine granularity to give precision measurements of electrons and photons. The hadronic calorimeters have full ϕ coverage for accurate missing energy measurements and are symmetric around the beam axis for uniform resolution.

The ATLAS calorimeters are sampling calorimeters, composed of alternating layers of absorbers and active media. As a particle passes through a sampling calorimeter it interacts with a high-density material, the absorber, and creates a shower of particles that then pass through the active medium, which measures some of the energy of the particles as they pass through it. Electromagnetic and hadronic showers in the ATLAS calorimeters are nearly completely contained in their volume, while only a fraction of the deposited energy is sampled in repeated measurements along the calorimeter depth. The thickness of the layers is optimized to provide good longitudinal sampling of the shower profile. If the shower is contained, then a sampling calorimeter calibrated for the various responses of the electromagnetically and hadronically interacting particles can measure the original particle's initial energy.

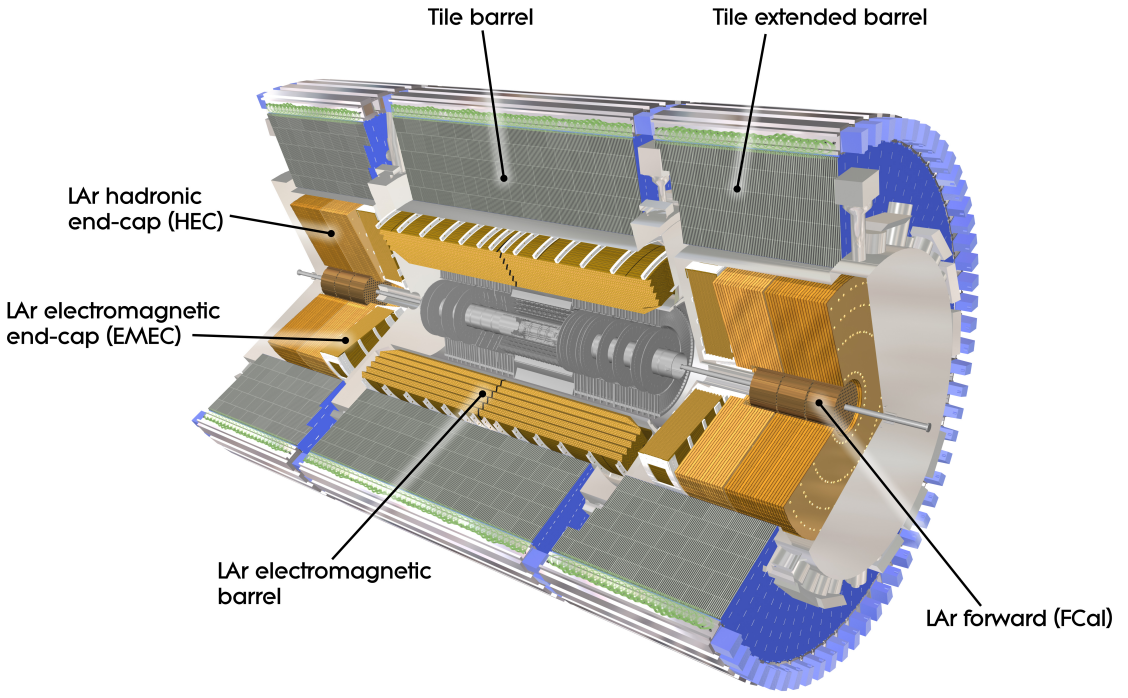

Figure 2.5: Cutaway diagram of ATLAS calorimeters showing its major components [1].

The liquid-argon calorimeters are so named because they use liquid argon (LAr) as the active medium. In this type of calorimeter, the liquid argon ionizes as a charged particle passes through it and the charges are picked up on electrodes to give an energy measurement. The tile calorimeter uses scintillator tiles as the active medium. These radiate ultraviolet photons when ionizing radiation passes through them and the light is collected to give an energy measurement.

The overall calorimeter system is composed of multiple sub-detectors. Both the electromagnetic and hadronic calorimeters are built with separate barrel calorimeter, end-cap calorimeters, and forward calorimeters. The hadronic calorimeter also has extended barrels that surround the end-cap electromagnetic and hadronic end-cap calorimeters. The electromagnetic calorimeters are all liquid-argon calorimeters and the hadronic calorimeters are made up of LAr calorimeters in the end-caps and the forward regions and tile calorimeters in the barrel. In summary the ATLAS calorimeter system is made up of the EM barrel, the EM end-caps, the tile barrel, the tile extended barrels, the hadronic end-caps, and the forward calorimeters as shown in

Figure 2.5. Since the cosmic muons in this analysis are required to pass through the inner detector and the rate of cosmic muons that traverse both the forward calorimeters and the inner detector is very low, the forward calorimeters will not be described any further.

2.2.1 Electromagnetic Calorimetry

The electromagnetic calorimeter consists of the barrel part ($|\eta| < 1.475$) and the end-caps ($1.375 < |\eta| < 3.2$). All of these are liquid-argon calorimeters and use an accordion fold geometry that naturally provides full ϕ coverage as shown in Figure 2.6. The absorbers are lead and follow the folds of the accordion shape while the electrodes are placed in the gaps between the sheets in a bath of liquid argon. In the barrel region the folds of the accordion geometry look like triangular waves and the peaks and troughs of these waves are located at constant radial positions. The angle of each bend changes with increasing radius to keep the gap between adjacent sheets constant. In the end-caps the triangular wave folds have peaks and troughs at constant z positions. This layout makes the gap between adjacent sheets increase with radius. The EM calorimeter is also supplemented with a presampler located outside the solenoid magnet and immediately in front of the EM calorimeter. It measures the energy lost by incident particles before they reach the calorimeter [3].

2.2.2 Hadronic Calorimeters

Tile Calorimeter

The tile calorimeter is located directly outside the envelope of the EM calorimeter. It is built as a barrel ($|\eta| < 1.0$) and extended-barrel ($0.8 < |\eta| < 1.7$). Unlike the EM calorimeter it uses steel as the absorber and scintillation tiles as the active media. The absorber-tile pattern is laid out radially and is normal to the beam axis. This pattern is common for both the barrel and the extended-barrel components.

Hadronic End-cap Calorimeter

The hadronic end-cap calorimeter ($1.5 < |\eta| < 3.2$) is a liquid-argon sampling calorimeter like the EM calorimeter but it does not share the same accordion geometry. The hadronic end-cap calorimeters use plates of the absorber material, copper,

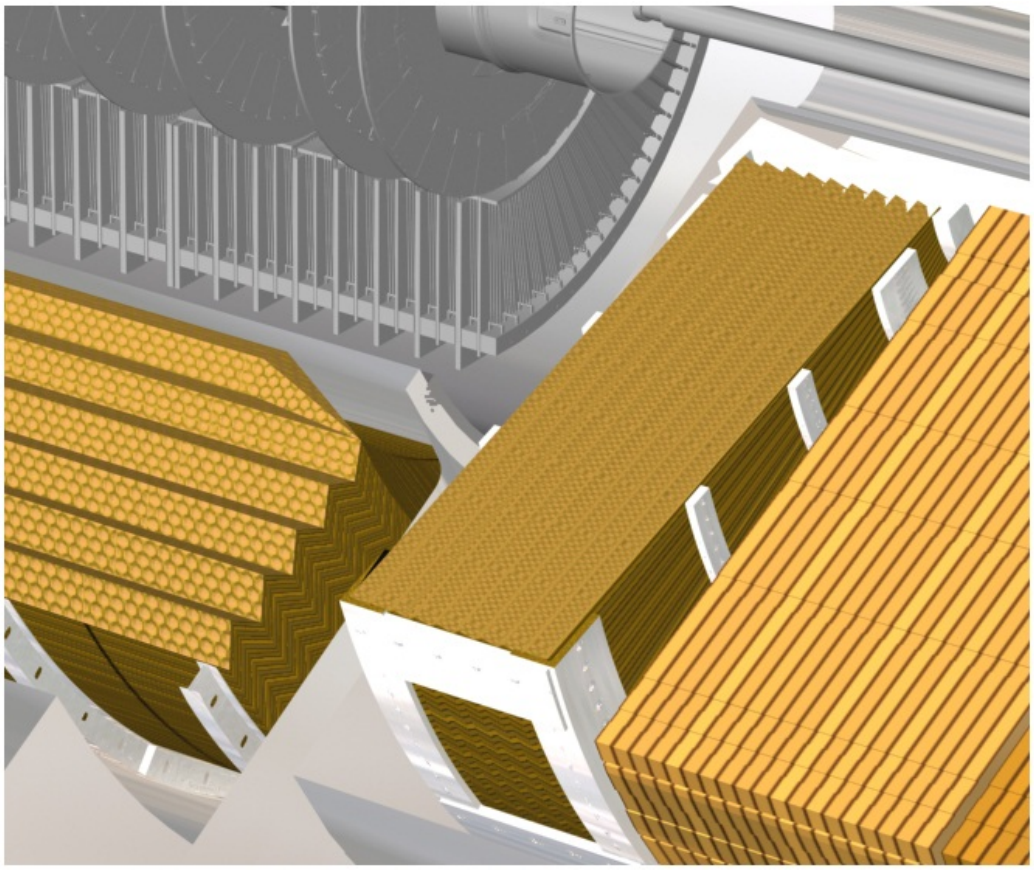

Figure 2.6: Part of the liquid argon calorimeters showing the accordion geometry of both the barrel and the end-caps [1].

with liquid argon in the gaps between them. These are assembled into wheels which are placed face-to-face along the z axis.

2.3 Muon Spectrometer

The ATLAS muon spectrometer was designed to help give ATLAS "good muon identification and momentum resolution over a wide range of momenta and the ability to determine unambiguously the charge of high-p_{T} muons [1]." To accomplish this the muon spectrometer makes use of four different types of detectors: monitored drift tubes (MDTs), thin gap chambers (TGCs), resistive plate chambers (RPCs), and cathode strip chambers (CSCs) as depicted in Figure 2.7. Three large superconducting air-core toroid magnets are used to deflect the muons' paths and enable the measurement of their charges and momenta (see section 2.4). The air-core de-

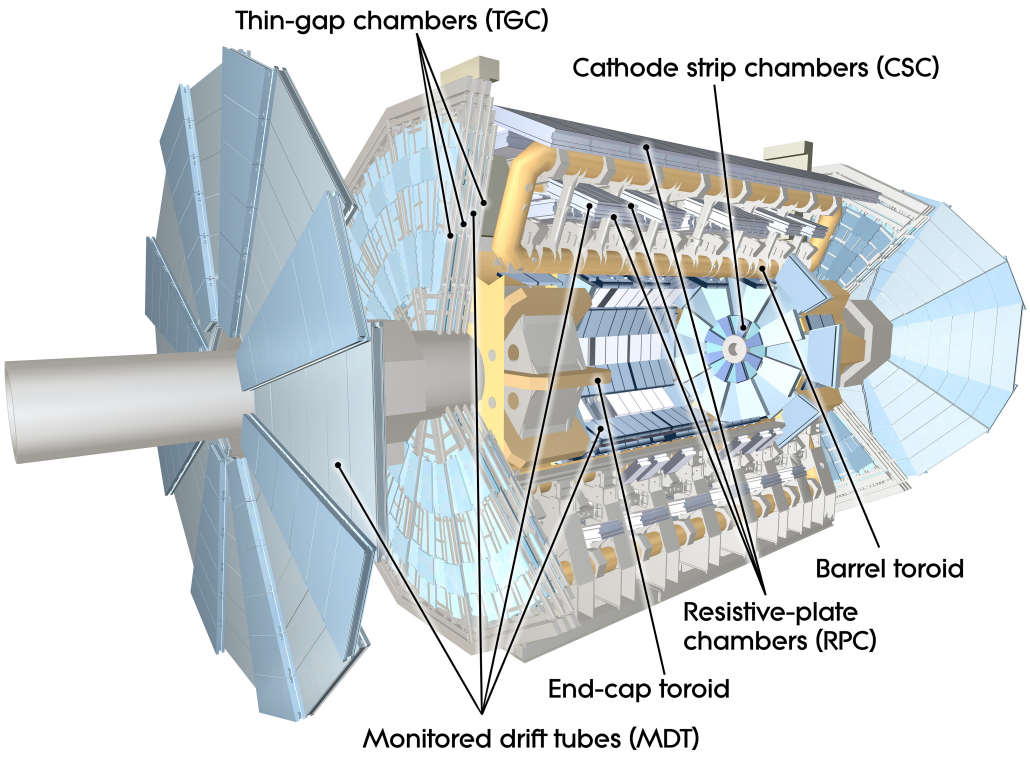

Figure 2.7: Cutaway diagram of ATLAS muon spectrometer showing its major components [1].

sign minimizes the amount of material that the muons traverse and so minimizes the resolution loss due to multiple scattering. The toroids were designed such that the magnetic field is roughly perpendicular to the trajectory of the muons and the bending of the muon tracks is in the r-z plane. The MDTs and CSCs are used to take precision measurements of the coordinates of track hits in the bending direction of the toroidal magnet (z in the barrel and r in the end-cap regions) and therefore give the muon momentum measurement ($|\eta| < 2.7$). The RPCs and TGCs are used for both triggering ($|\eta| < 2.4$) and measuring the track hit coordinates in the direction orthogonal to the precision measurement coordinate and approximately parallel to the magnetic field, the ϕ coordinate. The third position coordinate is known from detector alignments.

The different muon spectrometer detectors are arranged around the outside of the calorimeters such that particles from the interaction point traverse three layers (stations) of detector chambers. As shown in Figure 2.8 the chambers are arranged to form three concentric cylinders around the beam axis in the barrel region and in

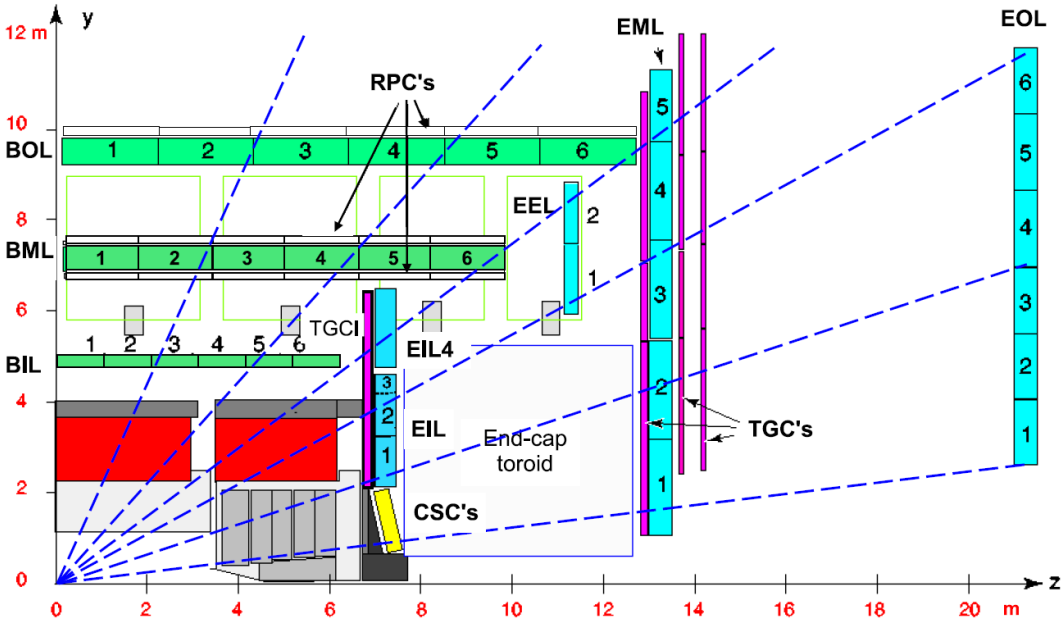

Figure 2.8: Layout of the muon spectrometer. The Barrel Inner, Middle, and Outer Layers, and the End-cap Inner, Extra, Middle, and Outer Layers are labelled for the MDTs. The general positions of the CSCs, RPCs, and TGCs are shown [1].

the end-cap regions the chambers are arranged in wheels that are perpendicular to the z-axis (they are in the x-y plane) [4]. The distances between the wheels allow for some η where it is only possible for a track to pass through two stations. To make sure that all tracks in the end-cap regions pass through at least three stations, an extra ring of detectors (not yet fully installed) is placed between the inner and middle wheels. Modules overlap to avoid gaps in the detector coverage, although there is a gap at $\eta \approx 0$ to allow for services to the solenoid magnet and the inner detector and for the cryogenic cooling pipes [5]. There are also holes for the feet of the detector (see section 2.5).

2.3.1 Monitored Drift Tubes (MDTs)

The monitored drift tubes are the main precision measurement detectors in the muon spectrometer. They cover the range $|\eta| < 2.7$ except in the innermost end-cap layer where they cover $|\eta| < 2.0$. An MDT is conceptually similar to the straw tubes of the TRT in the inner detector (see section 2.1.2). The analogue signal from a single MDT (a single drift tube) can take over a 100 ns to be processed by the analogue to

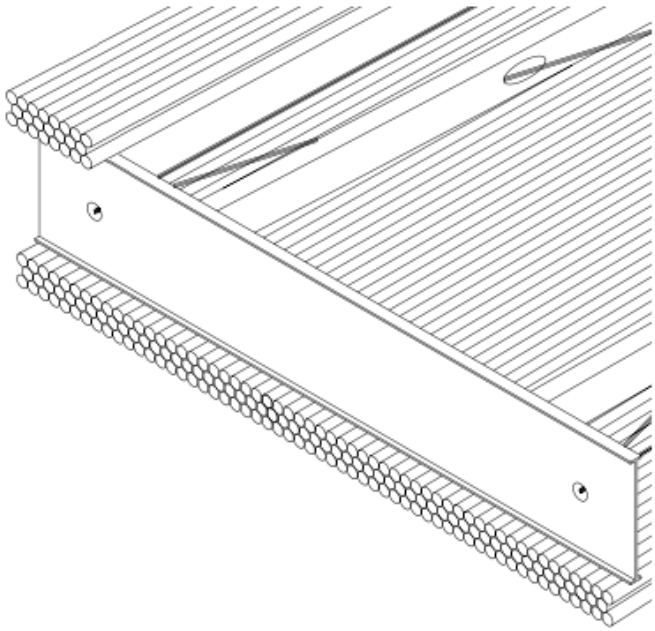

Figure 2.9: Geometry of the end of one of the muon spectrometer's MDT chamber from the barrel region showing the multilayers [5].

digital converter and the maximum drift time is 700 ns so a deadtime is applied to make sure there is no leftover signal in the electronics when the tube goes live again. This is a different deadtime than described in section 3.2.1.

In the layout of the muon spectrometer, tubes are arranged in planes or "monolayers" [5]. These monolayers are stacked in multilayers comprising three (in the middle and outer stations) or four (in the inner station) individual monolayers. Two multilayers are glued to an aluminum spacer to make a chamber. This chamber structure allows for a fit to be made on the hits in these layers to reconstruct two-dimensional track segments within each station. In the barrel the chambers are rectangular, as shown in Figure 2.9, and in the end-caps they are trapezoidal. In the barrel region the chambers are arranged in three concentric cylinders, so that particles will pass through the "inner", "middle" and "outer" stations. In the end-caps the chambers are arranged in four disks. In both the barrel and the end-caps the MDTs are oriented such that their axes lie tangential to circles around the beam axis. The average muon travelling outwards from the centre of the detector will traverse 2×4 MDTs in the inner station, 2×3 MDTs in the middle station, and 2×3 MDTs in the outer station totalling 20 MDT hits.

2.3.2 Cathode Strip Chambers (CSCs)

The cathode strip chambers are multiwire proportional chambers used for precision position measurements in the high η region of the detector ($2 < |\eta| < 2.7$). In the very forward regions of ATLAS there is a large flux of particles. These detectors were chosen to be used in this region because of their good time, spatial and double track resolution along with their high rate capacity [1]. The CSCs are organized into wheels; one in each end-cap.

2.3.3 Resistive Plate Chambers (RPCs)

The resistive plate chambers are the triggering detectors of the muon spectrometer used in the barrel region of $|\eta| < 1.05$. The RPCs are gaseous detectors and have two planes of strips: a cathode and an anode. The two sets of strips are orthogonal to each other.

The RPCs are mounted on common supports with the MDTs, which only measure the z coordinate of tracks in the barrel region. They provide the missing ϕ coordinate measurements and a coarse z measurement [1]. These detectors come in three stations and there are two layers of RPCs per station (a "doublet") as shown in Figure 2.10. Two of the RPC doublets are on the middle MDT station and the other RPC doublet is on the outer side of the outermost MDT station. As shown in Figure 2.8 the distance between the two innermost RPC doublets is small and the distance between the middle and the outer RPC doublets is large. These distances between RPC doublets help with triggering muons of different momenta (to be discussed in section 3.2.1).

2.3.4 Thin Gap Chambers (TGCs)

The thin gap chambers are mounted in concentric rings in the end-caps and are used for triggering and measuring the track hit ϕ coordinates to complement the MDTs precision position measurements. Around the middle wheel of MDTs there are seven layers of TGCs ($1.92 < |\eta| < 2.4$): two "doublets" and a "triplet". The TGC layer on the inner side of the outermost MDT layer is the triplet. In the inner layer of MDTs there is only a single doublet of TGCs ($1.05 < |\eta| < 1.92$). As with the RPCs there are gaps between the TGC doublets and triplets for triggering purposes. There are no TGCs in the outer MDT wheel (the ϕ coordinate can be extrapolated from the middle layer as there is no magnetic field to bend the particle trajectories in

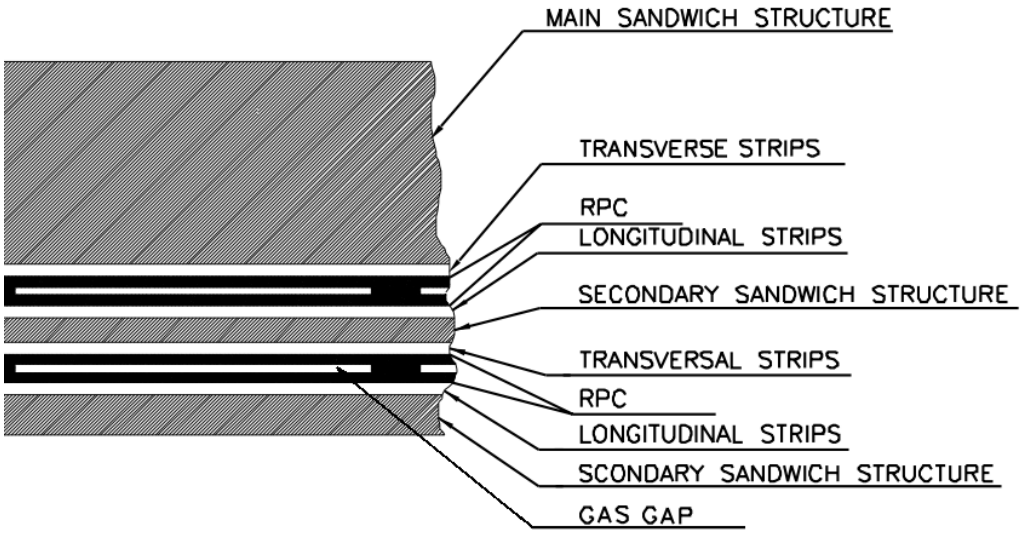

Figure 2.10: Geometry of the muon spectrometer's RPCs in a station [5].

that region). TGCs are multiwire proportional chambers like the CSCs. One cathode plane is segmented into strips while the wires run orthogonal to the strips. Both r and ϕ measurements are made by using the signals from both the wires and the strips.

2.4 Solenoid and Toroid Magnets

The ATLAS superconducting magnets, shown in Figure 2.11, are cooled to an operating temperature of 4.5 K and produce a magnetic field to bend the tracks of the particles. The central solenoid bends the tracks in the inner detector while the three toroidal magnets bends the muon tracks (in the r-z plane) in the muon spectrometer.

The solenoid is located between the inner detector and the calorimeters in the cryostat with the calorimeters. Since the EM calorimeter is situated immediately outside the solenoid, the magnet's windings are made to minimize as much as possible the number of interactions with traversing particles [7]. The solenoid assembly contributes approximately 0.66 radiation lengths for a particle traversing it at a normal angle [1]. When running with the nominal operational current of 7.73 kA the magnet has a stored energy of 40 MJ and produces a field of 2 T at the centre of the detector. Being far enough away from the surrounding toroidal magnets, its field is unaffected by the toroids' fields. It is, however influenced by the iron in the hadronic

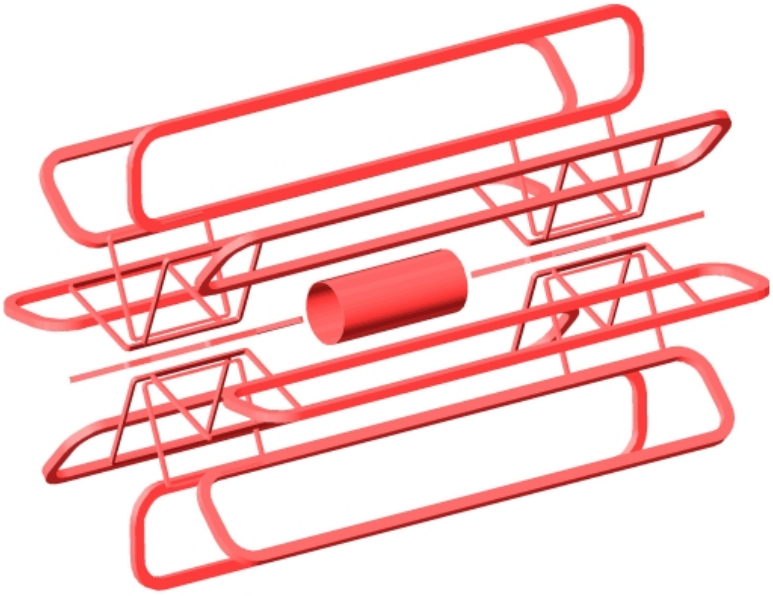

Figure 2.11: The ATLAS magnets: the solenoid, the barrel toroid, and the end-cap toroids [6].

calorimeter and the hadronic calorimeter's support system that act as a partial flux return for the solenoid's field [8].

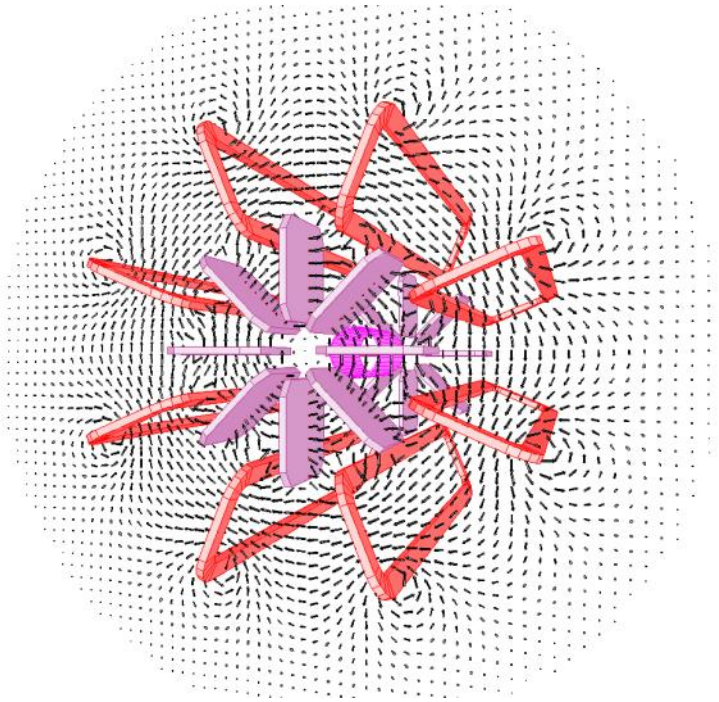

Figure 2.12: The magnetic field lines within an x-y plane [9].

Each of the three toroidal magnets is made up of eight flat coils assembled radially and symmetrically around the z-axis ($0 < |\eta| < 2.7$). The magnetic field they produce is approximately perpendicular to the trajectory of the muons as indicated in Figure 2.12. When the toroidal magnets are running with the nominal current of 20.5 kA the toroid in the central region produces a maximal field of 0.5 T and the end-cap magnets produce a maximal field of 1 T. The amount of stored energy is 1.1 GJ and 2×0.25 GJ in the barrel and end-cap magnets respectively [1].

2.5 Feet and Rail System

The main support system of ATLAS is the feet and rail system as shown in Figure 2.13. It is made up of nine pairs of feet bound by girders [1]. On top of the feet are two rails and their supports that carry the central part of the detector. Since the feet are between the bottom two toroid coils, which rest right on them, the feet are made of a stainless steel with a low magnetic permeability.

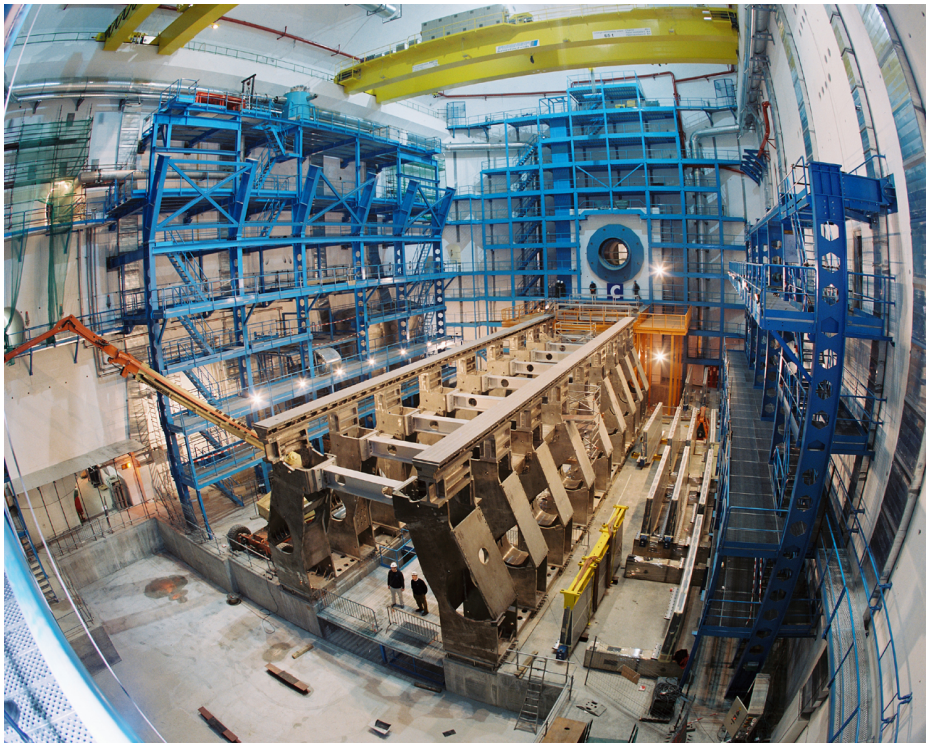

Figure 2.13: The feet and rail system that supports the central part of ATLAS [1].

2.6 The ATLAS Cavern and the Overburden

The floor of the ATLAS cavern is approximately 92 m underground and cosmic radiation has to traverse a substantial amount of material before it can be detected. The cosmic ray flux in ATLAS depends strongly on the geometry and geology of the overburden, buildings, caverns, and access shafts that the particles have to traverse.

ATLAS is located at Point 1 (of 8) along the LHC's circumference. Construction for the ATLAS experimental area started while LEP was still operating. The detector itself is housed in the main ATLAS cavern (UX15), which is 50 m long, 30 m wide, and 35 m high. This is connected to the surface by access shafts including the two main ones (PX14 and PX16), which are both 60 m deep, and 18 m and 12.6 m in diameter [1]. The main access shafts are used for the transfer of detector equipment to the experimental cavern. One is also fitted with air ducts for ventilation, which assist in the removal of 180 kW of heat released into the air of the cavern by the detector [1, 10]. These two access shafts are located directly above the detector as shown in Figure 2.14, and allow a higher rate of cosmic muons to hit the ATLAS detector than if there were only solid rock above it (to be discussed in section 5.1).

The cavern walls, roof, and floor along with the main access shafts' walls are lined with concrete over a metre thick [11]. Between 1995 and 1997 a geological investigation of Point 1 was performed determining the rock to be made up of sandstones, marls, and transitional rock types [12]. The surface buildings at Point 1 include SX1, a steel frame building located on top of the main access shafts. After construction was completed a slab of concrete was placed over the access shafts. All of these objects also affect the flux of cosmic muons in the different parts of the detector.

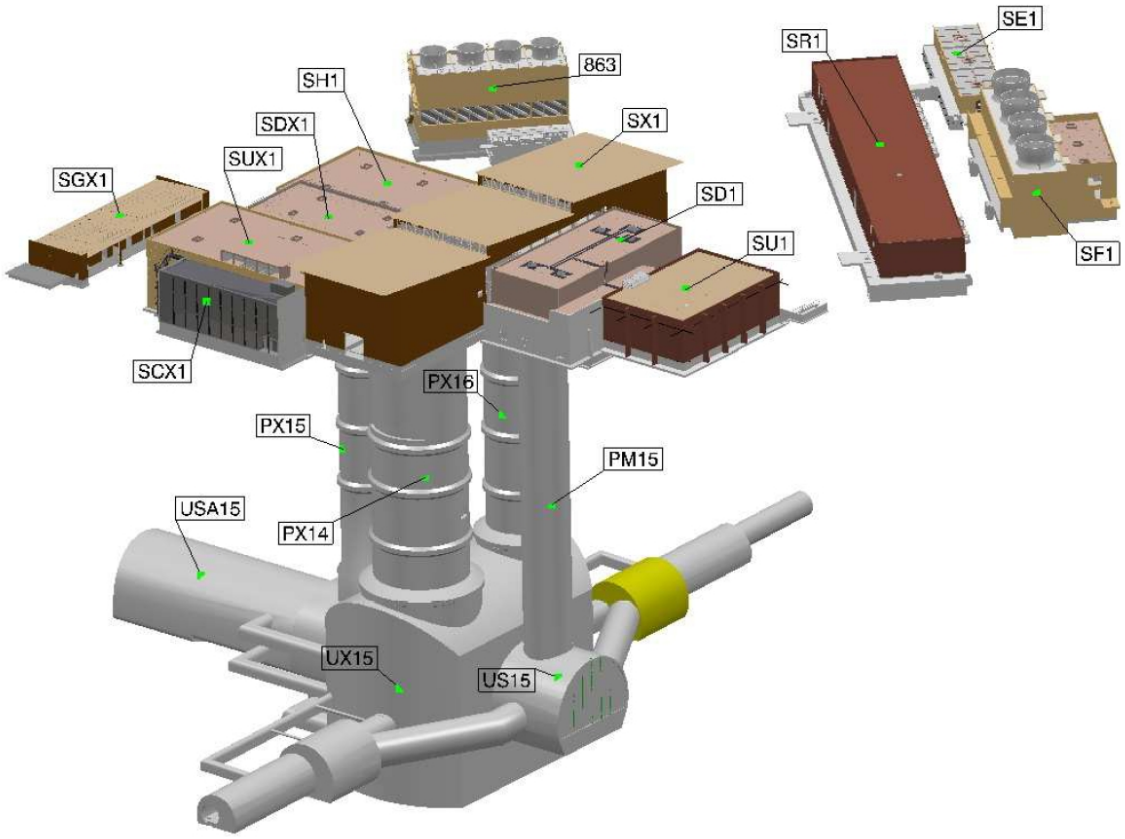

Figure 2.14: The surface buildings, access shafts, and main cavern of the ATLAS site [1].

Chapter 3

Timing and Triggering

3.1 The LHC Beam and Timing

The LHC is designed to run with up to 2808 proton bunches and to collide them at a rate of up to 40.08 MHz. This makes timing in ATLAS extremely important. To trigger on events ATLAS needs precise information on when the proton bunches or empty buckets cross in the detector. Time information is also important for the grouping of data for monitoring and analysis purposes.

3.1.1 LHC Filling Scheme and Bunch Groups

The LHC beams have a nominal bunch spacing of approximately 24.95 ns [13]. This is generated by the LHC's 400.8 MHz superconducting RF system. The RF system creates a series of RF buckets into which the proton bunches can be placed. In the nominal filling scheme every tenth RF bucket is filled, giving 3564 possible bunch positions of which up to 2808 can be filled [14, 15]. Not all positions are filled because gaps need to be left for beam dump purposes (an abort gap), injector chain constraints, and other operational reasons. Each intersection of two possible bunch positions at the centre of ATLAS is labelled with a Bunch Crossing Identifier (BCID), an integer between 0 and 3563. The BCID, as illustrated in Figure 3.1 resets after each beam orbit around the LHC.

The fill scheme specifies which BCIDs are used for what purposes. During a collision run, some BCIDs correspond to colliding pairs of proton bunches and some other BCIDs are "unpaired bunches": a filled bunch "colliding" with an empty bucket, used for background studies. The remaining BCIDs are empty. In the filling scheme, bunch

groups organize and label the different BCIDs [16]. In each fill scheme, a single BCID is part of one or more bunch groups; however, some bunch groups will never have an overlapping subset of BCIDs e.g. no BCID in the *filled* bunch group will also be in the *empty* bunch group. There are several bunch groups that label the unfilled BCIDs, one important one being the *empty* bunch group. The bunch positions in the *empty* bunch group are chosen to be several BCIDs away from any filled buckets so as to avoid contamination. The bunch groups are important for the central trigger processor of the level-1 trigger (see section 3.2.1). In dedicated cosmic runs there are no proton bunches in the LHC but the RF system and filling schemes are still used. The cosmic muons studied in this analysis are sought in the BCIDs of the *empty* bunch group. In a dedicated cosmic run there are many more BCIDs in the *empty* bunch group than in other runs. Aside from labelling which BCIDs contain proton bunches, some bunch groups are used for other purposes such as the *calibration requests* bunch group and the *bunch counter reset veto* bunch group.

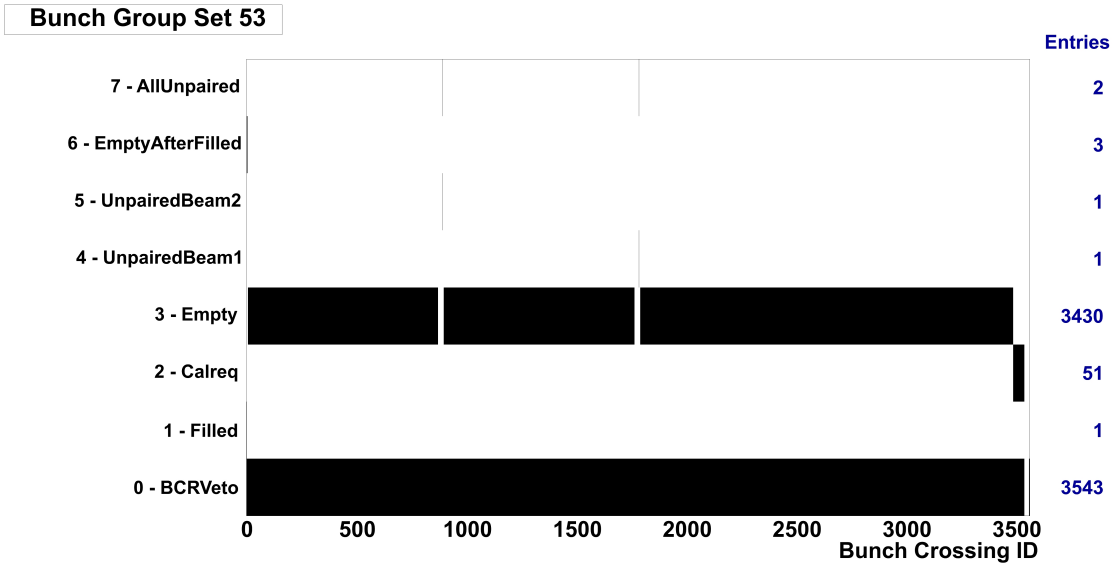

Figure 3.1: Sample fill scheme (run 152344) marking each BCID as being a member of which bunch groups. In this example, 3430 BCIDs are part of the *empty* bunch group. Even though there were no beams in the LHC for this run, one BCID is in the *filled* bunch group as well as one BCID in each of the two bunch groups for the unpaired proton bunches.

3.1.2 Luminosity Blocks

During data taking it is important to record information on the state of the detector. To do this ATLAS splits runs into many short time intervals for luminosity determination, data quality, and related monitoring processes [17]. One of these quanta of time is called a luminosity block (or "lumiblock"), a time interval for which the integrated, deadtime-corrected, and prescale-corrected luminosity can be determined [18].

The duration of a luminosity block is determined empirically from operation. The luminosity of the LHC is generally time dependent; however, the dependence is slow enough that it can be approximated to be constant over the short time span of a lumiblock. The amount of time it takes to calculate the luminosity is under a minute so the requirements of luminosity determination do not strongly affect the selection of the luminosity block duration. The duration of a lumiblock is mostly determined by the mean time between system failures and the details of the computing model [18].

If a detector ceases to function properly or there are other system errors then an analysis may exclude the associated luminosity blocks. Consequently, the shorter the length of a lumiblock, the less data will be excluded. The ATLAS computing model ensures that all the data from one lumiblock is collected together in the same file or set of files to reduce bookkeeping and complexity. As a result, the duration of a luminosity block is not strongly dependent upon the LHC beams but rather on the maximum file size to which the data is written, trigger bandwidth, and the number of processors available.

The duration of a luminosity block during a dedicated cosmic run is calculated in the same way as during a collisions run but with slightly different conditions to take into account. With no beam in the LHC there is no dependence upon luminosity. The duration of a luminosity block during a dedicated cosmic run is usually one or two minutes.

3.2 The Trigger System

The ATLAS triggering system is extremely important to the experiment's ability to filter and record data. Since hard scattering processes are quite rare, the triggering system is used to filter all the data and determine which events to save to disk. There

are three levels to the ATLAS trigger: Level-1 (L1), Level-2 (L2), and the event filter (EF) [1]. At the nominal bunch spacing of 25 ns the event rate in ATLAS is approximately 40 MHz. The level-1 trigger was designed to reduce the 40 MHz rate to 75 kHz (upgradable to 100 kHz). The L2 trigger was designed to reduce this to below 3.5 kHz and the event filter reduces it to the final rate of about 200 Hz, the rate at which the data is written to disk [17, 19]. The final raw event size is approximately 1.3 MB.

The level-1 trigger uses data from the calorimeters and the muon spectrometer, searching for signatures of high-p_{T} muons, electrons, photons, jets, and taus decaying into hadrons. The L1 trigger also searches for large total transverse energy and large missing transverse energy [1]. High-p_{T} muons are identified using the RPCs (barrel) and TGCs (end-caps) in the muon spectrometer (see section 2.3). The L1 calorimeter selections are made using reduced granularity information from all of the calorimeters. For each event the L1 trigger forms one or more regions of interest (ROI) that include information on the type of features identified and the criteria that caused the ROI to be formed. The ROI are then passed on to the level-2 trigger.

The L2 trigger uses all the available data in the ROI at full granularity and precision, and uses fast algorithms to reconstruct tracks within them. A single ROI contains approximately 2% of all the data in the event [1]. The event filter uses fully built events. This gives it access to information from the inner detector and so particle identification is significantly enhanced [20]. The L2 trigger and the event filter are collectively referred to as the High Level Trigger (HLT) and they are based almost entirely on commercially available computers and networking hardware.

3.2.1 The Level-1 Trigger

The level-1 trigger, shown in Figure 3.2, is based on custom-built electronics and uses information from the calorimeters and the muon spectrometer to filter out the events to pass to the level-2 trigger [17]. It is composed of several components, the main ones being the L1 Calorimeter Trigger (L1Calo), the L1 muon trigger, and the Central Trigger Processor (CTP). The L1Calo searches for indications of objects with high transverse energy such as electrons, photons, jets, tau-leptons decaying into hadrons, and events with large missing transverse energy. The L1 muon trigger searches for hit patterns that are indicative of high-p_{T} muons originating from the interaction region [1]. The L1Calo and the L1 muon trigger pass trigger object multi-

plicities and transverse energy threshold information to the CTP. The overall level-1 decision to pass the event on to the level-2 trigger, the L1 Accept Signal (L1A), is made by the CTP. During a run, most of the trigger settings cannot be changed, except for the trigger prescales and the bunch group, which can change only at luminosity block boundaries.

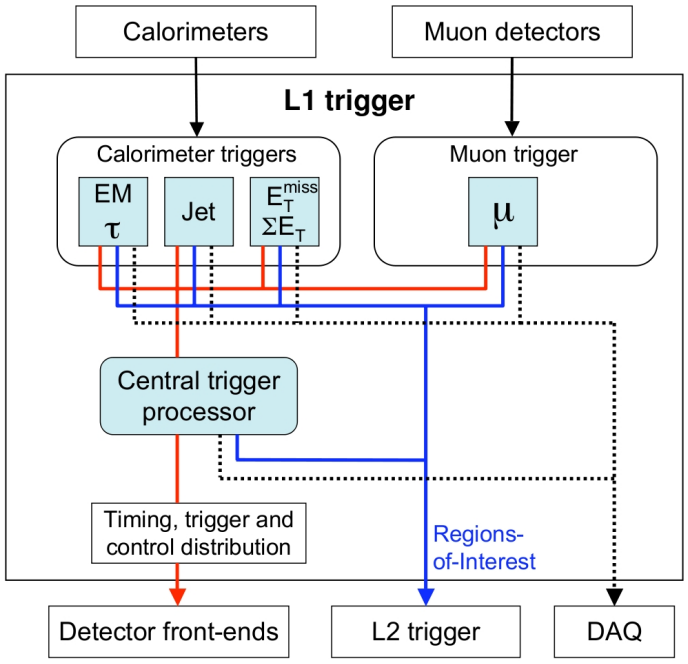

Figure 3.2: Block diagram of the level-1 trigger [1].

The Level-1 Muon Trigger

The L1 muon trigger processes the raw data from the muon spectrometer for up to two muon-track candidates per trigger sector including the position information and the p_{T} thresholds passed by the muon candidates. It combines all of this information from the different sectors and calculates total multiplicities for the different p_{T} thresholds while ensuring there is no double counting of muons that traverse more than one detector region [1, 21]. These multiplicities are forwarded to the CTP, which uses them when making the L1A. The time between bunches can be very short and the time of flight of the muons can be very long due to the size of the muon spectrometer so all the information from the detectors has to be retained in pipeline memories. The L1 muon trigger algorithms work very similarly in the barrel and end-cap regions. They search for muons originating from the interaction region by looking for

the coincidence of hits in the detectors.

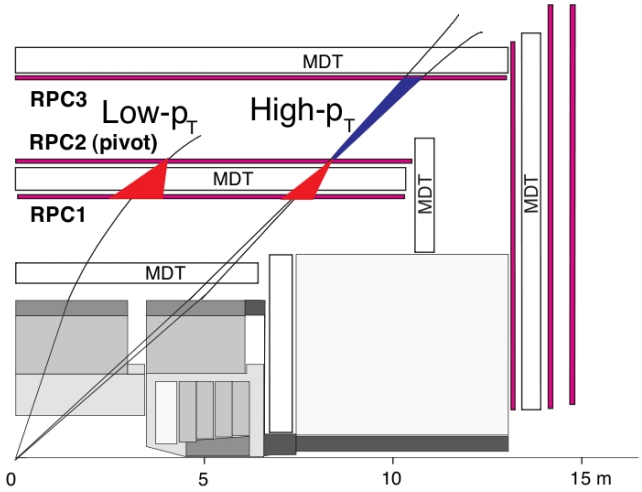

Figure 3.3: The RPC doublets with example low-p_{T} and high-p_{T} roads for the muon trigger [1]. The innermost layer of TGCs is not depicted.

In the barrel region the trigger detectors (RPCs) are arranged in three doublets as shown in Figure 3.3. The trigger is setup to trigger on low-p_{T} and high-p_{T} muons. The algorithm for the low-p_{T} thresholds works in the following way: if a hit is found in the second RPC doublet (the "pivot plane") then a search is performed in the first RPC doublet for a corresponding hit. This search is done within a road (or a "coincidence window") which is centred on a straight line (an imaginary infinite momentum track) between the hit in the pivot plane and the interaction point [1]. The width of the road depends on the p_{T} threshold of the trigger; the larger the size of the coincidence window, the smaller the p_{T} threshold. The coincidence window size also depends on other factors like the magnetic field, and the energy loss fluctuations and Coulomb scattering in the calorimeters. The exact sizes are determined using Monte Carlo simulations [19]. The algorithm works in both the η and ϕ projections so as to avoid accidentally triggering on low-energy particles in the cavern. To be able to reject fake tracks from noise, three of four layers have to register coincidence hits [1]. The length of the "lever arm" here spans the distance between the pivot and the other trigger plane.

The high-p_{T} thresholds algorithm is similar. It makes use of the low-p_{T} trigger built from the hits in the two inner doublets and includes information from the outer doublet. At least one of two possible layers of the outermost RPC doublet has to

register a hit [1]. A road is made following the line from that hit to the interaction point. The large space between the middle and the outer RPC stations allows the trigger to select the nearly straight tracks of high-p_{T} muons in the 11-35 GeV region. The smaller gap between the two inner RPC doublets allows the trigger to select the more curved tracks of low-p_{T} muons in the 6-10 GeV range [1]. For the high-p_{T} road the lever arm has the length of the distance between the pivot plane and the outer RPC station. It is the two sizes of the lever arms that allow for the low-p_{T} and high-p_{T} roads for the muon trigger.

In the end-cap regions the TGCs are used as the trigger detectors and are arranged into three doublets and one triplet. The trigger algorithm for the end-caps works in a similar way to that for the barrel. The outermost TGC doublet is used as the pivot plane and again coincidence hits are required for the three low-p_{T} and three high-p_{T} thresholds [1]. For both the low and high-p_{T} thresholds, the number of coincidence hits per plane, the coincidence window size, and which plane is used as the pivot greatly affect the efficiencies of the thresholds of the L1 muon trigger.

The Central Trigger Processor, Prescales, and Deadtime

The Central Trigger Processor is the last stage of the level-1 trigger and its purpose is to reduce all the trigger information to a single bit, the L1 Accept Signal [17]. The CTP also provides an absolute GPS-based UTC timestamp that can be used to correlate data with other sources. It receives information from the L1 calorimeter trigger and the L1 muon trigger about particle and jet multiplicities, and which thresholds were passed for total and missing transverse energy and total jet transverse energy [1]. It also receives information from special triggers for various purposes such as the bunch group identification (see section 3.1.1). Up to 372 input signals can be received by the CTP but it can only transmit 160 signals internally and so a selection is made from the input signals. To make the L1A several steps are taken in the CTP as shown in Figure 3.4.

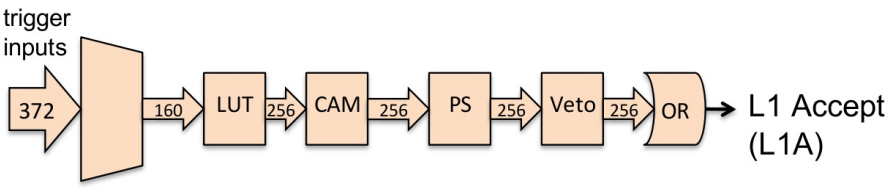

Figure 3.4: The path through the Central Trigger Processor [17].

The first step after the input signals have been reduced is to use look-up tables (LUTs) to produce up to 256 trigger conditions [17]. Content-addressable memories (CAMs) combine these trigger conditions to form up to 256 triggers where every trigger condition can contribute to every trigger. All of the level-1 muon triggers for the *empty* bunch group follow the same naming convention: "L1_MU∗_EMPTY", where the ∗ is replaced by the p_{T} threshold (in GeV) e.g. L1_MU6_EMPTY.

In the next step the prescales are applied to the different triggers. A prescale factor, PS, is a number that tells the trigger how frequently it should accept a particular trigger. If a trigger has a prescale of n then only 1 in every n times will the trigger be passed. This is used to selectively reduce the rate of the common events that swamp the interesting rare processes. Prescales can be changed during a run but only on luminosity block boundaries.

Next, in the Veto step, deadtime and busy signals are combined to make veto signals for the different triggers. Deadtime is the time period when valid L1As are vetoed to prevent uncontrolled memory overflows. There are two kinds of deadtime: simple and complex [22]. Complex deadtime is introduced to prevent an overflow in the buffers of the front-end systems. The trigger applies complex deadtime by enforcing that there be no more than n L1As in m possible bunch crossings [23]. Simple deadtime is applied whenever there is an L1A. The trigger applies simple deadtime by enforcing that there are no L1As for n possible bunch crossings after each L1A. The CTP is the only place in ATLAS that implements deadtime. The fractional amount of deadtime over a certain duration, typically one lumiblock, is referred to as the Deadtime Fraction. The deadtime fraction for each trigger can be approximated by

$$k_i^{\mathrm{DT}} = 1 - \frac{N_i^{\mathrm{AV}}}{N_i^{\mathrm{AP}}}, \tag{3.1}$$

where N_i^{AV} is the number of times in luminosity block i that the L1 trigger fired as counted immediately *After the Veto* step in the CTP. N_i^{AP} is the number of times in luminosity block i that the L1 trigger fired as counted immediately *After the Prescale* step in the CTP.

In the final step in the CTP all the level-1 signals are combined to make the L1 accept using the OR operator [17].

3.2.2 Data Streams

ATLAS uses a data streaming model that stores raw data in one or more files depending on the trigger decision. Each stream consists of events that pass one or more trigger signatures and is grouped with similarly triggered events. Data streams are chosen to have approximately the same number of events in each stream with less than 10% event duplication between streams [4]. The streams include an express stream, which is used for monitoring, a minimum bias event stream, and a cosmic muon stream. The cosmic muon stream includes all the events where a L1 muon trigger fired for an *empty* bunch group, e.g. L1_MU6_EMPTY.

3.2.3 Triggering on Muons from Cosmic Radiation and from Collisions

The level-1 trigger system in ATLAS is designed and calibrated for muons from collisions but cosmic muons will still cause the triggers to fire. In general, the muon triggers for the *empty* bunch group work exactly the same way as the muon triggers for the *filled* bunch group for collisions. A very important point for this analysis is that ATLAS triggers on cosmic muons in the same way as on muons from collisions [24]. The trigger roads are set up assuming that muons originate from the interaction region and are not adjusted for cosmic muons that travel along less projective trajectories.

The timing requirements of the trigger algorithms are also calibrated for muons from collisions and not adjusted for cosmic muons. The hit signals are internally aligned by applying 3 ns delays so that the hits belonging to the same particle arrive at the same time at the input of the chip performing the trigger algorithm. These delays take into account various factors including the time of flight of muons, cable lengths, and processing time. Cosmic muons in the upper half of ATLAS travel the "wrong way" or "backwards in time" with respect to muons from collisions. In the upper half of ATLAS the trigger arms of the low-p_{T} roads are short enough (see section 3.2.1) that the time of flight of the cosmic muons is negligible and the low-p_{T} road trigger algorithms are always satisfied. For cosmic muons in the upper half of ATLAS the high-p_{T} road trigger algorithms are less likely to be satisfied because the length of the trigger arm is so large that the time of flight is larger than 3 ns and the hit signals in the innermost and outermost RPC stations will not be aligned. In the lower half of ATLAS the cosmic muons travel in the "correct direction" and so there are no problems with the high-p_{T} road triggers.

The triggering situation for cosmics is made more complex because a single cosmic muon has the potential to fire a trigger in both the top and the bottom halves of ATLAS. The time difference between a muon trigger firing in the top and bottom halves of ATLAS is approximately the duration of two bunch crossings. During a collision run, if a cosmic muon were to cause a trigger to fire in the top half of ATLAS, the simple deadtime applied by the CTP would prevent the muon from firing a trigger in the lower half of ATLAS because the duration of the simple deadtime is longer than the time of flight of the muon (see section 3.2.1). The information on the second trigger candidate is, however not lost because the level-1 barrel readout window lasts the duration of 8 bunch crossings. During a dedicated cosmic run the trigger setup can be changed to align the trigger signals from the RPCs in the upper and lower halves of ATLAS to remove the time of flight time difference.

Chapter 4

Particle Track Reconstruction

Before any analyses can be performed the raw data have to be reconstructed to build the particle tracks and determine the identity of the particles. For muons this is done using data from most of the detector. Track candidates are first reconstructed in the inner detector as well as in the muon spectrometer and then combined tracks are made using information from the inner detector, the muon spectrometer, and the calorimeters.

4.1 Inner Detector Tracks

The tracks of charged particles with $p_{\mathrm{T}} > 0.5$ GeV and $|\eta| < 2.5$ are reconstructed and measured in the inner detector and magnetic field generated by the solenoid [1]. The reconstruction process in the inner detector can be divided into three steps. First, in the pre-processing stage, raw data (electric charges and currents) from the pixel and SCT trackers (see section 2.1.1) are converted into clusters of signal information. A cluster of sensor information is used because the hit position resolution improves if the signal is deposited over several pixel (or SCT) sensors. The data from the SCTs have to be clustered because two silicon microstrips are required to measure the third coordinate. The raw data from the TRT (see section 2.1.2) are converted into drift circles where a drift circle is a radial position of the track's distance from the central anode wire. In the track-finding stage, partial tracks are formed using the hits in the first few silicon detector layers closest to the beam pipe. The track fits are cleaned up by removing outlying hits and fake tracks are rejected. The data are then refitted and these steps are iterated by including more hits and then drift circles until the final

track candidates are created. In the final step the reconstruction algorithms perform a search for vertices (the interaction points from which the particles emanate).

4.2 Muon Spectrometer Tracks

The reconstruction process in the muon spectrometer can be separated into four steps: pre-processing, pattern-finding and segment making, segment combining, and track-fitting [1]. In the first step the raw data are used to form drift circles in the MDTs and clusters in the CSCs, RPCs, and TGCs (see section 2.3). Track segments are built by making short track fits within single MDT or CSC stations. Fully fledged track candidates are built from track segments and the final track fitting takes into account in almost full detail the geometry of the material that the muons traverse and the inhomogeneities of the magnetic field along the muons' trajectories. The tracks are then extrapolated back to the interaction point and the momentum is corrected for the energy lost in the calorimeters. A muon typically loses about 3 GeV, mainly due to ionization, in the material between the inner detector and the muon spectrometer although high-p_{T} muons occasionally deposit a very large fraction of their energy via bremsstrahlung radiation. To make the proper corrections to the reconstruction the extrapolation package combines tools for propagating muons through the active and passive material of the full detector.

4.3 Combined Tracks

To maximize the p_{T} resolution, a statistical combination of the track candidates in the muon spectrometer and in the inner detector is used for $|\eta| < 2.5$ (the geometric acceptance of the inner detector) [1]. These tracks are called "combined tracks" and in this analysis only combined tracks formed using the STACO muon tracking algorithm [25, 4] will be used.

Using both the inner detector and the muon spectrometer to reconstruct a track offers optimal momentum resolution over a wide range of muon momenta. For muons in the 6-100 GeV momentum range, both the inner detector and the muon spectrometer are used [26]. Momenta below 30 GeV are determined primarily by the inner detector because the muon spectrometer resolution is dominated by multiple Coulomb scattering. For muons with momenta below about 6 GeV the muon spectrometer is used only for identification because the muons often do not reach the middle and outer

stations [1]. To achieve the required performance the inner detector and the muon spectrometer have to be both aligned and calibrated internally and with respect to each other. The reconstruction efficiency for muons is reduced in some regions of the detector due to holes in the acceptance geometry of the muon spectrometer. These holes may be dead channels or actual gaps in the muon spectrometer for the feet and in the $\eta \approx 0$ region (see sections 2.3 and 2.5) [1].

4.4 Reconstruction of Muons from Cosmic Radiation and from Collisions

The reconstruction of cosmic muons is similar to the reconstruction of muons from collisions but does not require the cosmic muon tracks to originate from the central region of the detector and (as a result of this) uses different timing requirements [27]. In proton-proton collisions the tracks produced emanate from (or near) the interaction region and are said to be "projective". In cosmic events the muons always travel downward and most of them will not pass through the interaction region; however, with a large enough sample of cosmic muons a few will pass near the centre of the detector and be approximately projective. These few muons are said to be "pseudo-projective".

In the upper half of the detector the cosmic muons are travelling the "wrong way" or "backwards in time" with respect to muons from collisions. As a result, special versions of the reconstruction algorithms are written for dedicated cosmic runs to allow for the different directions of the muons' trajectories in the upper half of the detector. Since the reconstruction algorithms for collision events only expect projective muons it is possible that the part of a cosmic muon track that is in the upper half of the detector may not be triggered or correctly reconstructed. If a cosmic muon track traversing the detector around the time of a bunch crossing is not reconstructed in the upper half of the detector but is reconstructed in the bottom half of the detector then the event may appear to have missing transverse energy. Cosmic events where this happens would be a background to studies that look for events with muons and missing energy [28] (see section 5.3).

The tracks from cosmic muons differ from those of muons from collisions because cosmic muons can traverse the top *and* bottom halves of the detector and so the reconstruction algorithms are written to accommodate cosmic muon tracks that are

potentially twice as long as and have twice as many detector hits as projective muon tracks. For dedicated cosmic runs the full length of a pseudo-projective cosmic muon track is not reconstructed as a single track. The reconstructed track is made using detector hits from both the upper half ($y > 0$) of the inner detector *and* the lower half ($y < 0$) of the inner detector but only the upper *or* the lower half of the muon spectrometer. The reconstruction algorithms, when reconstructing data from collisions, fit the data in the upper half ($y > 0$) of the detector separately from the data in the lower half ($y < 0$) of the detector. This means that a single cosmic muon may be reconstructed by the "collisions" reconstruction algorithms as 0, 1, or 2 muon tracks.

In general the reconstruction efficiency can be very different for cosmic muons than for muons from collisions because the trajectories of cosmic muons do not require them to traverse any minimum amount of the detector. A muon that hits only a single MDT in the outer layer of the muon spectrometer will of course not have a reconstructed track. To force the cosmic muons being studied to travel similar paths to projective muons the track perigee cuts are centred around a small area near the centre of the detector (see d_0 and z_0 cuts in section 6.2.2). The reconstruction efficiency for cosmic muons is approximately constant in the central region of the detector but drops off as $|d_0|$ and $|z_0|$ increase because the experiment is optimized for looking at collision data emanating from the central region of the detector. These pseudo-projective tracks will have an associated reconstruction efficiency that can be approximated to be the same as the reconstruction efficiency for projective tracks. In this analysis the cosmic muons were reconstructed with reconstruction algorithms specially adapted for cosmic radiation.

Chapter 5

Muons from Cosmic Rays and Proton-Proton Collisions

Cosmic rays were the first introduction scientists had to particles not found in the atom and it was from cosmic rays that the muon was discovered. The muon is unique amongst charged particles because it has a relatively long mean lifetime, doesn't have strong interactions, and at cosmic ray energies is minimum ionizing. Muons are commonly studied in ATLAS analyses because they provide a good signal that a hard scattering process took place in the event. When cosmic rays reach the Earth's surface, many of the particles are muons. Cosmic muons are of interest to particle collider experiments because they can penetrate large amounts of material and be detected by experiments like ATLAS and therefore form a background to muons from collisions.

5.1 Cosmic Ray Theory

Cosmic rays were discovered through their power of ionization [29]. At the top of the atmosphere, cosmic radiation is composed of all the charged particles and nuclei with lifetimes of the order or greater than 10^6 years. When these particles interact with nucleons in the atmosphere they create other particles. These newly produced particles can also interact or decay creating a cascade of particles through the entire depth of the atmosphere as shown in Figure 5.1. Cosmic muons are created primarily through the decay of pions and kaons that were created in the interaction of cosmic rays with atmospheric nuclei.

At sea level, the muon is the most abundant charged particle component of secondary cosmic radiation [30] ("secondary cosmic radiation" is discussed in section 5.1.1). The muon mean lifetime is 2.197 μs but due to the cosmic muons' high energies and time dilation they usually travel a large distance before they decay. As is generally true for all particles, the flux of muons will decrease with increasing penetration depth; however, muons can penetrate farther into a material than most other particles. In the Earth's atmosphere, the muon's typical production height is approximately 15 km. A muon only requires an energy above $\sim$ 2.5 GeV for its decay length to be longer than its production height. Most muons produced high in the atmosphere lose only approximately 2 GeV to ionization before they reach the ground [2]. At sea level the vertical intensity of cosmic muon for energies above 20 GeV is 2.9 s^{-1} m^{-2} sr^{-1} [30, 31]. Assuming the intensity of cosmic muons follows $I(\theta) = I(0)\cos^2(\theta)$ then the flux of cosmic muons at sea level for energies above 20 GeV is 6.0 s^{-1} m^{-2} covering the range $\theta < 75\,^\circ$, where θ is the angle from the zenith [2, 30].

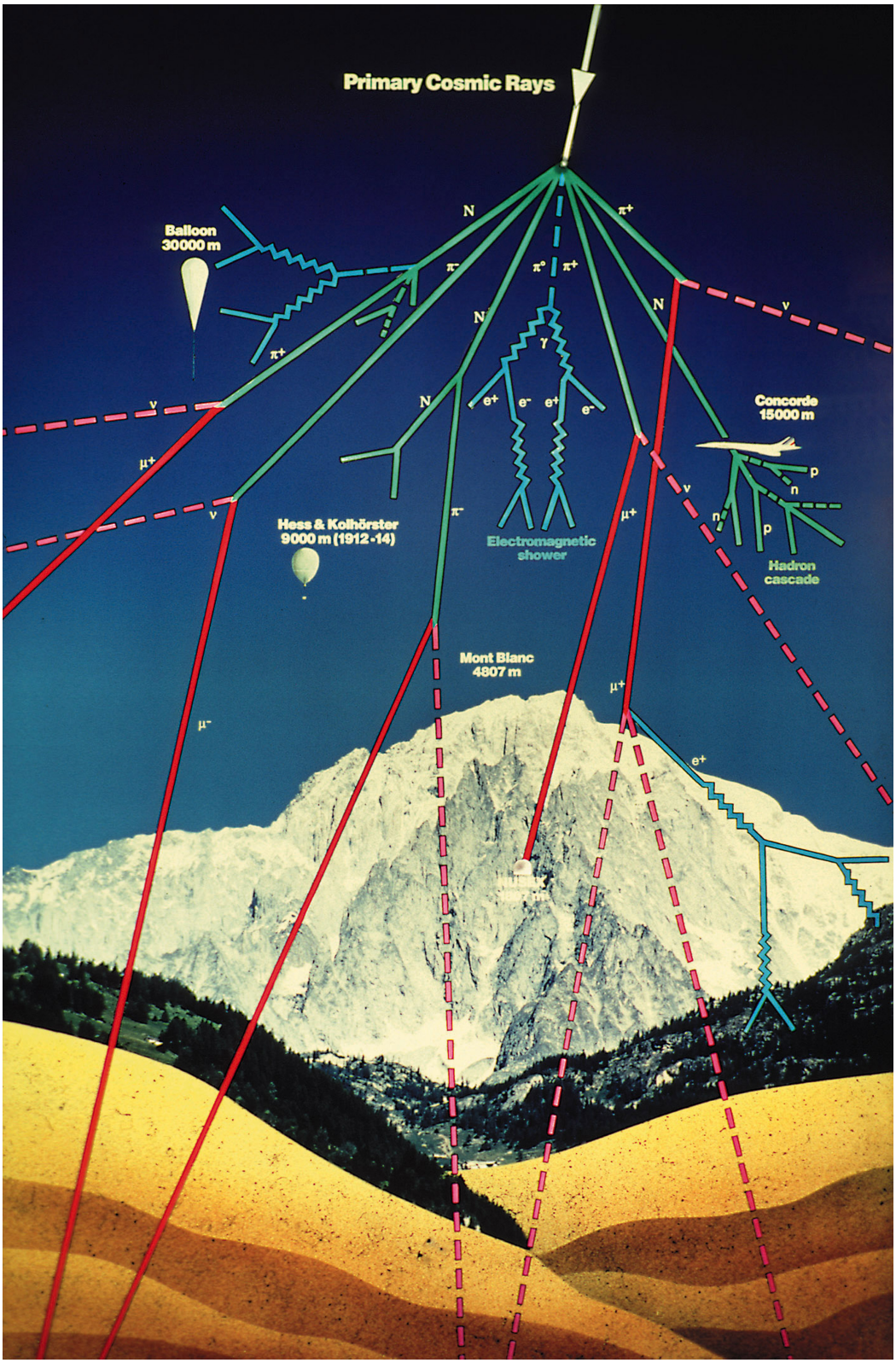

Figure 5.1: Cosmic cascade [32].

5.1.1 Primary and Secondary Cosmic Rays

With the exception of solar flares, the origins of most cosmic ray particles are outside the solar system [2]. Cosmic rays are classified as either primary or secondary. Primary cosmic rays are from astronomical sources and commonly composed of electrons, protons, and the nuclei of atoms e.g. helium, carbon, oxygen, iron and other nuclei synthesized in stars. Secondary cosmic rays are produced in interactions of primary cosmic ray particles with interstellar gases. They include the nuclei of atoms like lithium, beryllium, and boron, which are not abundant end-products of stellar nucleosynthesis.

Early intensity measurements made in the equatorial region showed that more cosmic radiation enters the atmosphere from the west than from the east. This was an indication that the major part of the cosmic radiation was composed of positively charged particles with trajectories being bent by the Earth's magnetic field [29]. Approximately 79% of the primary cosmic rays are free protons and about 70% of the rest are helium nuclei. This implies that most primary cosmic rays are composed of protons and neutrons. There is also a non-zero flux of anti-protons but it is small with an anti-proton to proton ratio of approximately 2×10^{-4} at energies around 10 to 20 GeV [2]. Most cosmic rays are relativistic with energies comparable to or greater than their rest masses. A small fraction have ultrarelativistic energies extending up to 10^{20} eV, which is 11 orders of magnitude above the proton's rest mass energy.

The flux of cosmic rays depends on a multitude of factors. The trajectories of the charged particle component of the cosmic rays are bent by the different magnetic fields in the solar system. The cosmic ray flux is also affected by the Sun through solar flares and the Sun's alternating 11 year sunspot cycle [2]. The sunspots appear in pairs where one sunspot generally has a magnetic field polarity that is the opposite of the other sunspot. The polarities reverse at the start of each new sunspot cycle thus making the true period of solar activity 22 years [29]. With the Earth's atmosphere and magnetic field, and all the other factors included, the cosmic ray flux thus depends on altitude, longitude, latitude, temperature, time, and several other variables. However, to first order the cosmic ray flux can be considered constant in time at sea level [33] and this approximation will be used for the entirety of this study.

The cascade equations (also known as "diffusion equations" or "transport equations") describe the propagation of particles through the atmosphere. They depend on the particles' properties, their interactions, and the structure of the atmosphere

[34]. More precisely, the coupled, one dimensional cascade equations that properly account for interactions where the incoming and outgoing particles can be of different types are:

$$\frac{\mathrm{d}N_i\left(E_i, X\right)}{\mathrm{d}X} = -\left(\frac{1}{\lambda_i} + \frac{1}{d_i}\right) N_i\left(E_i, X\right) + \sum_j \int_{E_i}^{\infty} \frac{F_{ji}\left(E_i, E_j\right)}{E_i} \frac{N_j\left(E_j, X\right)}{\lambda_j} \mathrm{d}E_j, \quad (5.1)$$

where X is the "slant depth", which is measured from the top of the atmosphere along the direction of the incident particle. The flux of particles of type i at depth X in the atmosphere and energy between E_i and $E_i + \mathrm{d}E_i$ is represented by $N_i\left(E_i, X\right)\mathrm{d}E_i$. For particles of i, d_i is the decay length and λ_i is the interaction length in air. The dimensionless inclusive cross-section (integrated over transverse momentum) for an incident particle of type j and energy E_j to collide with an air nucleus producing a particle of type i with energy E_i is represented by $F_{ji}\left(E_i, E_j\right)$. The quantities X, λ_i, and d_i are all measured in g/cm^2.

Solving this system of equations gives the flux for each particle type. The results can be used to calculate the production spectrum for each of the secondaries. One commonly used approximation is to assume that the differential equations are separable: $N_i\left(E_i, X\right) = g_i\left(X\right) G_i\left(E_i\right)$ and that the energy part is proportional to $E_i^{-(\gamma+1)}$. For energies less than approximately 10^6 GeV it is found that $\gamma \approx 1.7$ [34].

The cascade equations can be solved analytically to give the particle fluxes but only for very simple approximations. In general the systems under study are extremely complex and so in practice numerical integration or Monte Carlo simulations are used to solve the cascade equations to produce theoretical estimates of the particle fluxes.

Cosmic Muons Underground

For cosmic muons to reach the ATLAS detector they must first traverse the overburden. Some of the cosmic muons will travel to the detector partly through the main access shafts and so those muons' energy spectrum may be similar to the cosmic muon energy spectrum at the surface. The rest of the cosmic muons will traverse various amounts of rock in the overburden and lose some of their energy through ionization and radiative processes: bremsstrahlung, pair production, and photo-nuclear interactions. Cosmic muons generally have mean energy loss rates close to the minimum and hence are minimum-ionizing particles [2] and the rock of the overburden will filter

out part of the lower end of the cosmic muon energy spectrum.

The total energy loss relations for muons can be written as a function of the amount of material that the particles traverse

$$-\frac{dE}{dX} = a(E) + b(E)E \tag{5.2}$$

where $a(E)$ is the ionization loss and $b(E)$ is the fractional energy loss by the three radiative processes [2]. Both $a(E)$ and $b(E)$ are slowly varying functions of energy. For moderately relativistic muons the $a(E)$ term is given by the Bethe-Bloch formula (see [2] for full details). In practice these parameters are sensitive to the chemical composition of the rock and must be evaluated for each location. In the case of ATLAS the cosmic muon energy spectrum is complex because the cosmic muons can traverse such a wide range of distances through the overburden because of the access shafts.

5.1.2 Cosmic Muon Charge Ratio

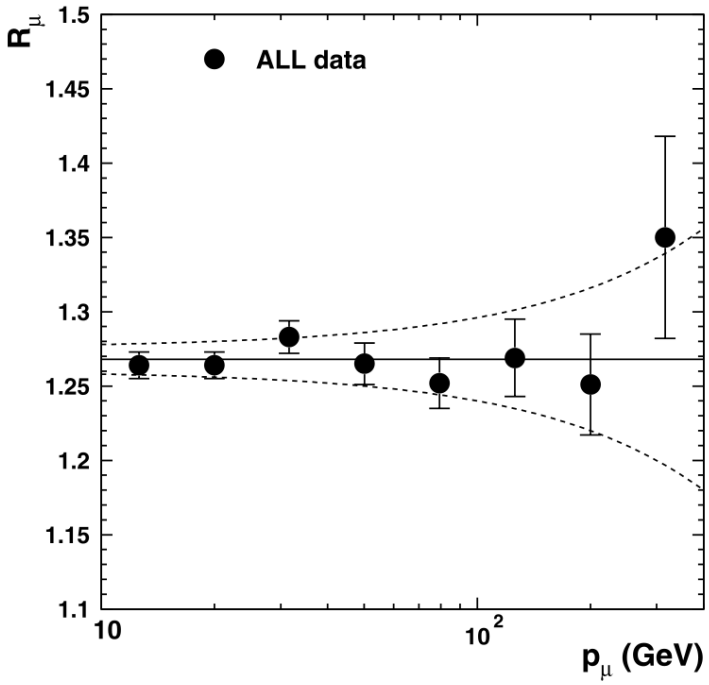

Figure 5.2: World average of the cosmic muon charge ratio [35].

The fluxes of positively and negatively charged cosmic muons are not the same.

The cosmic muon charge ratio, the ratio of the number of positively charged cosmic muons to the number of negatively charged cosmic muons has been experimentally measured to be approximately 1.2-1.3 for energies in the range of a few GeV all the way up to 1 TeV [36]. A world average of the cosmic muon charge ratio for muon momenta above 10 GeV at the Earth's surface has been calculated to be $1.268 \pm \left(0.008 + 0.0002\frac{p}{\text{GeV}}\right)$ using all the published data available at the time [35]. Here the uncertainty is given as a function of momentum. This ratio has several prominent features that are best studied by looking at a simplified model that describes the muon spectrum [36].

For this very basic model (see [36] for more details) it is assumed that the primary spectrum is composed only of protons that interact once with the atmospheric nuclei producing pions that all decay into muons. It is also assumed that there are no kaons produced that would contribute to the muon spectrum. Since the majority of the cosmic radiation comes in the form of protons, it is assumed that the only reactions that produce pions come from proton-proton collisions. With a few more approximations the cascade equations can be solved and the resulting pion flux is

$$\pi^{\pm}\left(E_{\pi}\right) \propto {E_{\pi}}^{-(\gamma+1)} Z_{p\pi^{\pm}} \tag{5.3}$$

where

$$Z_{p\pi^{\pm}} = \int_{0}^{1} F_{p\pi^{\pm}}\left(x_L\right) {x_L}^{\gamma-1} \mathrm{d}x_L, \tag{5.4}$$

$x_L \approx E_{\pi}/E_p$, and each particle's symbol is used to represent the flux for that particle type. This leads to the simple muon charge ratio:

$$\frac{N_{\mu^+}}{N_{\mu^-}} = \frac{\mu^+\left(E_{\mu}\right)}{\mu^-\left(E_{\mu}\right)} = \frac{\pi^+\left(E_{\mu}\right)}{\pi^-\left(E_{\mu}\right)} = \frac{Z_{p\pi^+}}{Z_{p\pi^-}} \tag{5.5}$$

The first feature to note is that the cosmic muon charge ratio in equation 5.5 is explicitly independent of the muon energy (this can also be seen in Figure 5.2). The second feature to notice is that $\frac{N_{\mu^+}}{N_{\mu^-}} > 1$, which in this model is a result of the fact that in general the incoming cosmic radiation flux at the top of the atmosphere consists mostly of positively charged protons (in this exaggerated model the initial cosmic radiation flux consists *only* of protons) and so more positively charged pions are likely to be produced than negatively charged pions due to charge conservation $\left(F_{p\pi^+}\left(x_L\right) > F_{p\pi^-}\left(x_L\right)\right.$ and therefore $Z_{p\pi^+} > Z_{p\pi^-}$ and ${}^{N_{\mu^+}}/_{N_{\mu^-}} > 1\left.\right)$.

5.2 Proton-Proton Collisions Theory

In ATLAS the two LHC proton beams are collided and a wide range of interactions can take place. Hard scattering processes only take place in a small fraction of the collisions at the LHC and the scattering processes possibly producing the Higgs boson or new heavy particles will be even more rare.

5.2.1 Minimum Bias Events

In the LHC the rare processes are the ones that ATLAS was built to study. They must be found amongst the very common minimum bias events. The number of minimum bias interactions per event is strongly dependent upon the luminosity. In 2011 for up to the end of June there were, on average, approximately six minimum bias interactions per event but this could increase to more than twenty minimum bias interactions per event when the LHC is running at design energy and luminosity [4, 37].

The term "minimum bias events" refers to events selected with a very loose trigger, i.e. the biases (or requirements) used to define an event are minimal. The term "minimum bias" is experimentally defined and slightly different definitions are made by each experiment. Factors like a detector's acceptance and triggers are used in making each experiment's definition of minimum bias events [4]. The vast majority of minimum bias events do not contain any tracks with large transverse momentum nor any large energy clusters in the calorimeters. Instead, most of the activity in these events are in the forward regions or lost down the beam pipe.

5.2.2 ATLAS Physics

At the LHC only a tiny fraction of the events will involve the hard scattering processes from the Standard Model or potential new physics. Muons are important particles in the current ATLAS analyses because they will be more common in the interesting hard scattering processes than in the background. This is especially true for muons with high p_{T} that are isolated from other activity in the detector [4]. Muons are used in several different analyses including studies of top quarks, Standard Model gauge bosons, and new particles from theories of physics beyond the Standard Model.

W and Z Bosons

The W and Z bosons from the Standard Model are the mediators of the weak force. They have relatively large production cross-sections and ATLAS has already seen many W and Z boson candidates in the early years of its physics program. W and Z bosons only decay via the weak force. Studies of these bosons are often done by looking for the decays of the W and Z bosons into electrons, muons, and neutrinos: $Z \to \mu\mu$, $Z \to ee$, $W \to e\nu$, $W \to \mu\nu$ [4]. These bosons usually decay into hadrons but also decay into leptons relatively frequently. The branching ratio for decays to muons is approximately 10% for the W and 3% for the Z [2]. These branching ratios are exactly the same for decays into electrons.

Top Quark

The top quark was discovered in 1995. It is the heaviest known quark in the Standard Model and has such a short half-life that it decays without forming hadrons and almost entirely through the single mode $t \to Wb$ [4]. Occasionally this W will decay into a muon and a neutrino.

Higgs Boson

The Higgs boson is the last remaining particle in the Standard Model yet to be discovered and the search for this particle is the main raison d'être of ATLAS and the LHC. Since it has not yet been discovered, previous experiments have only been able to place limits on the expected mass for this particle. Different masses of the Higgs boson imply different primary decay channels and so several different searches for the particle are used at the LHC. Some decay channels that involve the production of one or more muons include:

$H \to ZZ^{(*)} \to \ell\ell\ell\ell$,

$H \to \tau\tau$ and $\tau \to \ell\nu\nu$, and

$H \to W^+W^- \to \ell\nu\ell\nu, \ell\nu qq$, $(\ell = e, \mu)$ [4, 38].

W' and Z' Bosons

There are many theories for physics beyond the Standard Model. Several theories predict new weak interactions and new gauge bosons such as Little Higgs models,

Kaluza-Klein models, and technicolor models [4, 39]. Some of the simplest extensions of the Standard Model predict new neutral and charged gauge bosons referred to as Z' and W' respectively. The masses of these new bosons are not predicted but searches for them have been conducted and new gauge bosons have been ruled out for masses up to about $1.1 - 1.7$ TeV where the exact limit is model dependent [40, 41]. The LHC and ATLAS will extend the search for masses up to around 5 to 6 TeV. These bosons, as indicated by their names, resemble the W and Z bosons of the Standard Model and depending on the model, they may decay in similar ways. Searches for the W' involve looking for signals of a lepton plus missing transverse energy and searches for the Z' bosons include looking for dilepton resonances.

5.3 Cosmic Muons in Proton-Proton Collisions

Cosmic muons are constantly being detected by ATLAS. Their detection can be useful for tasks like aligning detectors but they may be mistakenly seen as a collision product when they are detected at the same time as a proton-proton collision. One cosmic muon background to the rare hard scattering process events, which produce particles like the elusive Higgs boson, is when a pseudo-projective cosmic muon track is in the detector at the same time as a minimum bias event. The probability of cosmic muons and a proton-proton collision faking an event with a hard scattering process depends on the number of muons expected for that type of event. The probability of a cosmic muon and a minimum bias event faking the signature of a Z is much higher than the probability of a cosmic muon (or cosmic muons) and a proton-proton collision faking a $H \rightarrow ZZ^{(*)} \rightarrow \ell\ell\ell\ell$ process. Different physics searches will have different cosmic muon backgrounds and the higher the cosmic muon flux, the larger the cosmic muon background will be.

Chapter 6

Analysis Method

Over the last few decades many experiments have measured the flux of cosmic muons. With the ATLAS detector the calculation of the flux is slightly complicated by the fact that ATLAS was built to study collisions, not cosmic radiation. Everything from the triggering system to the particle reconstruction algorithms are built for measuring particles originating from the central part of the detector and have to be slightly adjusted to study cosmic radiation.

6.1 Analysis Tools

Two main software tools were used to perform the cosmic flux analysis, Athena and ROOT. Athena is the ATLAS reconstruction and analysis framework that processes the ATLAS data at all levels to ensure that all geometry and conditions are consistent at all stages of the analyses [26]. It is a C++ (and Python) object-oriented code used for the analysis of both data and simulated samples. The same program is also used to generate the Monte Carlo samples and handle all samples data reconstruction. In this analysis, Athena version 16.0.3.4 was used. The Athena analysis outputs are stored in ROOT files [42]. ROOT is a commonly used, general purpose, stand-alone data analysis program. Part of the analysis was performed in ROOT and it was also used for its statistics and plotting features.

6.2 Data Selection

Generally the LHC and the ATLAS collaboration maximize the amount of time that the ATLAS detector is collecting collisions data. Usually when there is no beam the triggering system is put into cosmics mode to record cosmic ray data. The detector is made up of millions of parts and is extremely complex so it has to be constantly monitored and the operating conditions documented. For each analysis an input dataset has to be selected from all the ATLAS data by specifying the appropriate operating conditions.

6.2.1 Run Selection

Multiple requirements were placed on the data before being accepted for use in this analysis. First, all data used had to be taken during a dedicated cosmic data run for consistency in the run setup. No beams were allowed to be in the LHC during the dedicated cosmic runs to avoid contamination of the cosmic muon data. Dedicated cosmic runs can also be set up so that any events that pass the level-1 trigger will automatically pass the level-2 trigger and event filter. To ensure that the muons' momenta could be measured and to reproduce the detector settings used during collisions, both the solenoid and toroid magnets had to be running with nominal currents (see section 2.4). Avoiding large fractional amounts of deadtime is important in a flux calculation for the purpose of statistics and accuracy (see section 3.2.1). This is managed in part by requiring that the prescales for the triggers are only a little larger than one. A very low prescale (e.g. a prescale of 1) would allow the associated level-1 trigger to saturate and a very large prescale (e.g. a prescale of 8000) leaves too few muons to give statistically significant results. The deadtime fraction for a particular trigger also depends on the level-1 acceptance rate of all the other triggers. For this analysis the data triggering and level-1 acceptance rates should be roughly constant as should be the deadtime. Time periods with large spikes and variations in the deadtime that are on the same scale as the deadtime fraction itself are avoided. To simplify analyses and reduce computation time the ATLAS data are split up into different streams (see section 3.2.2). All data used in this analysis came from the *cosmicMuon* stream. It contains all the muons triggered by L1_MU∗_EMPTY (see section 3.2.1). All the runs used were required to have collected several tens of thousands of events to avoid analysing runs where only a few cosmic muons would pass all the cuts.

Some of the most important data checks were for data quality. ATLAS has groups

that look at the data and flag subsets of them where there were problems. The automatic monitoring and the data quality checking are done per luminosity block. This is true even for dedicated cosmic runs where there are no beams in the LHC (see section 3.1.2). In this analysis, only the luminosity blocks flagged as good were used and all other lumiblocks were skipped. Long time periods of several consecutive lumiblocks with constant settings, deadtimes, and trigger rates are used to ensure that the detector is in a state of stable running. This is an extra level of data quality checking because the data quality shift workers may, for various reasons, compare the cosmic data numbers and distributions to the expected collision data numbers and distributions and then submit the wrong data quality flags. At the same time, when settings are being changed frequently it can be a sign that the experiment shift workers are testing, calibrating or experimenting with different detector functions and not focusing on taking good cosmic data.

For the purposes of reconstruction and consistency, all of the parts of ATLAS required to detect the muons being studied in this analysis had to be functioning properly in the data used. Only the detectors in the barrel region were required. It is rare for a cosmics muon to pass through both an end-cap and the central region of the inner detector (see position cuts in section 6.2.2) and so the end-caps are not required in this analysis. The detectors required to be functioning properly include the MDTs and RPCs in the muon spectrometer, and the SCT and pixel trackers of the inner detector.

Other checks of the data quality were performed using the results of the analysis. The profiles of the detector-hits histograms were studied to ensure that the detector was functioning as expected and that the muons were reconstructed properly.

6.2.2 Event and Muon Selection Cuts

Most of the muon selection cuts are applied to ensure a minimum level of data quality for the analysis. Whenever possible, the cuts made in this analysis were selected to match those used for the first ATLAS $W' \rightarrow \mu\nu$ search as the cosmic background is relevant to this search (see section 5.2.2) [43].

Not all of the events studied in the analysis will have muons in them and some events may have several muons in them. Before any cuts are applied to the muons, cuts are applied to the events to first test if there are any muons in them. One of the first cuts applied was at the event level: a trigger cut. In this analysis, the

L1_MU6_EMPTY trigger was required to fire (see section 3.2.1). This trigger was chosen because the ATLAS collaboration has thoroughly studied its associated filled bunches level-1 trigger [44]. Selecting 6 GeV as the threshold was done in conjunction with the selection of a minimum p_{T} (discussed later in this section).

A low-p_{T} threshold is used because cosmic muons are much less likely to fire the high-p_{T} triggers for acceptance and timing reasons. The timing requirements of the triggering algorithms are calibrated for muons from collisions and cosmic muons are unlikely to meet these requirements in the upper half of ATLAS (see section 3.2.3). High-p_{T} roads are also very narrow and long. The acceptance for cosmic muons is lower for high-p_{T} roads because the less projective trajectories of the cosmic muons are less likely to pass through the entirety of the longer lever arm formed (see section 3.2.3). A high-p_{T} muon from a beam collision will travel along a straighter path through the detector and the trigger identifies these muons by using narrower roads (see section 3.2.1). Cosmic muons do not have to traverse the interaction region and so using a narrower road will not only reject low-p_{T} muons but also higher-p_{T} muons travelling along less projective trajectories.

The threshold for the trigger used in this analysis was also chosen not to be so low that every single muon entering the detector would be triggered upon. The L1_MU0_EMPTY trigger accepts a large number of low-p_{T} muons because the p_{T} distribution is heavily weighted towards low-p_{T} muons (see section 5.1.1 and to be discussed in more detail in section 7.2). It is heavily prescaled because otherwise its trigger firing rate would be large compared to the maximum allowed L1A rate. As a result very few of the recorded muons that fired the L1_MU0_EMPTY trigger pass all the cuts in this analysis. Another cut was made to ensure that the reconstructed muon track was a "combined" track (see section 4.3), with hits in both the inner detector and the muon spectrometer. The rest of the cuts made are specified in Table 6.1.

While the *empty* trigger requirement implicitly imposes cuts on the BCIDs, not all of the BCIDs in the *empty* bunch group can be used. The last 119 BCIDs of the orbit (BCIDs 3445-3563) are empty and used as an abort gap for beam safety. During this abort gap the detectors perform special tasks such as calibrations. The *empty* bunch group can overlap the abort gap and so those overlapping BCIDs are cut from the analysis.

In cylindrical coordinates a position can be partly specified using d_0 and z_0 as shown in Figure 6.1. The z position of a point is given by z_0 while d_0 is the radial

Table 6.1: Primary Muon Selection Cuts.

Cut Description	Cut
$\lvert d_0 \rvert$ (of perigee)	≤ 250.0 mm
$\lvert z_0 \rvert$ (of perigee)	≤ 500.0 mm
Number of SI (pixel+SCT) hits	≥ 12
Number of SCT hits	≥ 12
Number of MDT hits	≥ 10
p_{T} (at perigee)	≥ 20.0 GeV
BCID (before abort gap)	≤ 3444

position but with a sign matching that of the y coordinate of the Cartesian coordinate system, indicating whether the point is in the upper half or lower half of ATLAS. In this analysis these two variables specify the position of the *perigee* of a track (the point of closest approach of the track to the z axis).

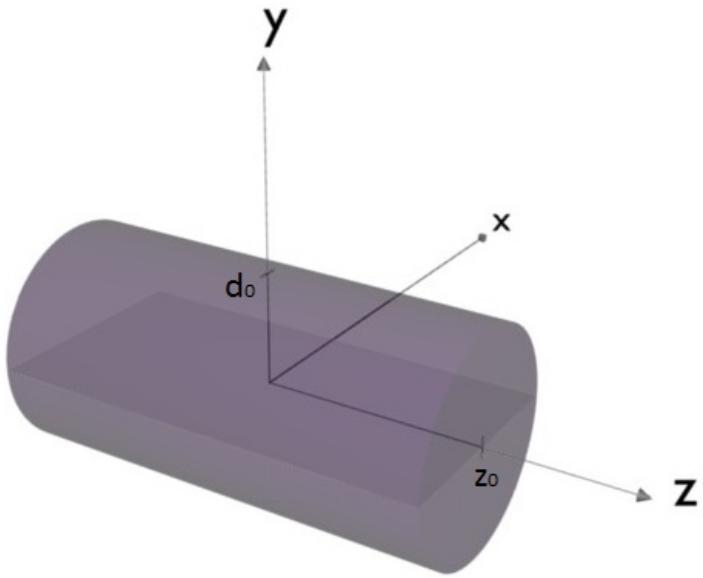

Figure 6.1: Cylinder defined by d_0 and z_0. The d_0-z_0 plane is visible along the x-z plane. See Table 6.1 and Figures 2.3 and 2.4 to see the volume and location of the fiducial region within the detector.

The d_0 and z_0 cuts are used to force each track's perigee to be within a maximum cylindrical volume defined by the cuts and to ensure that the reconstruction

efficiencies are approximately constant as a function of these variables. Since ATLAS is set up to detect particles travelling outwards from the centre of the detector, the reconstruction efficiencies drop if the track's perigee is too far from the centre of the detector (see section 4.4).

The maximum d_0 value (see Table 6.1) gives a position in between the outermost pixel layer and the innermost SCT layer (see Figures 2.3 and 2.4). The maximum z_0 value gives a position in the pixel end-cap wheels.

Hits in the inner detector and in the muon spectrometer are required to ensure a minimum quality of the track reconstruction. The p_{T} cut was selected to be large partly to match the p_{T} cuts from other analyses but also to ensure that the trajectories of the muons were fairly straight. This allows for a simple mapping of where the muon traversed the overburden. The value of the p_{T} cut and the threshold of the L1 muon trigger were chosen such that the p_{T} cut is several GeV larger than the threshold of the trigger to ensure that the trigger efficiency does not depend on p_{T}. An example of an L1_MU6 trigger turn on curve showing the plateau is displayed in Figure 6.2.

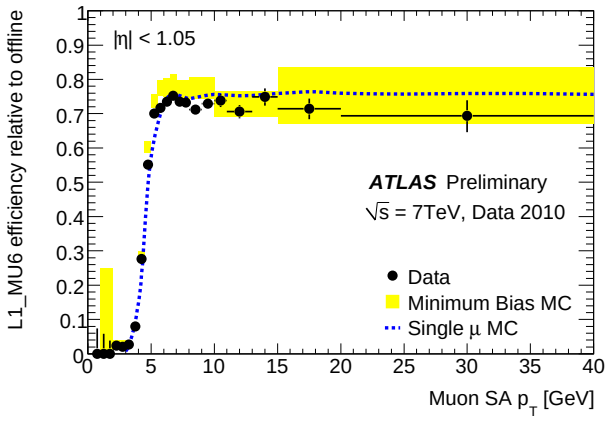

Figure 6.2: Turn-on curve for the L1_MU6 trigger in the barrel region only (RPCs) [45]. The transverse momenta is calculated using the muon spectrometer "stand alone". NOTE: This is only an example plot; it is not the same turn-on curve from which the trigger efficiency was calculated.

6.3 Flux Calculation

The cosmic muon flux is a useful quantity in the study of the backgrounds to rare hard scattering processes that include high-p_{T} muons. The higher the cosmic muon flux, the larger the cosmic muon background will be. The cosmic muon flux varies

slightly over the different regions of the detector and cavern but is approximately constant over the small area under study. The majority of particles from collisions originate near the centre of the detector and so it is here where it is most important to measure the cosmic muon flux. While the actual value of the flux depends upon the materials and geometry of the overburden, the measurement of the flux depends mostly on detector settings and efficiencies. The flux of muons is

$$\Phi_\mu \equiv \frac{1}{A}\frac{N_\mu}{\Delta t}, \tag{6.1}$$

where A is the cross-sectional area through which the particles pass, N_μ is the actual number of muons traversing the detector and Δt is the time interval during which the data were taken. In this analysis the area is taken to be

$$A = \left(2d_0^{\text{cut}}\right)\left(2z_0^{\text{cut}}\right) \tag{6.2}$$

where d_0^{cut} and z_0^{cut} are the cuts on the track perigee as defined in section 6.2.2 and with values given in Table 6.1. This equation gives the area of a plane in the x-z plane at $y = 0$ centred at the origin of the ATLAS coordinate system as shown in Figure 6.1. The fiducial area for the flux measurement is defined by $\pm d_0^{\text{cut}}$ and $\pm z_0^{\text{cut}}$.

It should be noted that by using the three-dimensional position of the perigee as a cut, an approximation is being made for the flux of the muons through the d_0^{cut}-z_0^{cut} plane; however, this should not greatly affect the results because of the high-p_{T} cut and downward trajectory of the majority of the muons.

The definitions for N_μ and Δt are slightly complicated by detector effects. To calculate the actual number of muons that traverse the detector and meet the cuts, the number of muons recorded must be scaled to account for inefficiencies and prescales. The actual number of muons is therefore

$$N_\mu = \frac{1}{\epsilon_{\text{trig}}}\frac{1}{\epsilon_{\text{rec}}}\sum_{i\in G} k_i^{\text{PS}} N_i^{\mu_{\text{meas}}}, \tag{6.3}$$

where ϵ_{trig} is the trigger efficiency and ϵ_{rec} is the reconstruction efficiency (see sections 3.2.1 and 4). In this definition it is assumed that only one trigger is used to accept muons with one associated prescale and that the high-level trigger is in pass-through mode meaning that it rejects no events. The prescale used for the trigger during luminosity block i is represented by k_i^{PS}. The set of all the lumiblocks that passed the data selection cuts defined in section 6.2 is represented by G. The number of muons

in luminosity block i that were recorded and passed the selection cuts is $N_i^{\mu_{\text{meas}}}$.

The effective time, Δt over which muons are recorded is calculated by correcting the luminosity block durations for the short time periods when the detector was not able to accept the trigger:

$$\Delta t = k^{\text{wind}} \sum_{i \in G} k_i^{\text{BCID}} \left(1 - k_i^{\text{DT}}\right) \Delta t_i, \tag{6.4}$$

where Δt_i is the duration of luminosity block i. The *time window fraction*, k^{wind}, is the fraction of time that the detector is allowed to record data around each beam crossing. The time window during which the detector can record data includes a period of time before and after the crossing of two buckets in ATLAS. Since cosmic radiation can enter the detector at any time, it can be detected before the beams cross, unlike the particles resulting from collisions. For all the data used in this analysis, $k^{\text{wind}} = 1$.

In luminosity block i the fraction of BCIDs that are suitable for the analysis, k_i^{BCID} is:

$$k_i^{\text{BCID}} \equiv \frac{N_i^{\text{empty}} - N_i^{\text{abort}}}{N^{\text{BCID}}}, \tag{6.5}$$

where N_i^{empty} is the number of BCIDs in the *empty* bunch group (see section 3.1.1) and N_i^{abort} is the number of BCIDs that are in the *empty* bunch group but overlap the abort gap. The total number of BCIDs is $N^{\text{BCID}} = 3564$.

The last element of the Δt definition is k_i^{DT}, the deadtime fraction for luminosity block i (see section 3.2.1).

The cosmic muon flux definition in the fiducial region can be expanded by combining expressions 6.1, 6.3, and 6.4 resulting in

$$\Phi_\mu = \frac{1}{A} \frac{\frac{1}{\epsilon_{\text{trig}}} \frac{1}{\epsilon_{\text{rec}}} \sum_{i \in G} k_i^{\text{PS}} N_i^{\mu_{\text{meas}}}}{k^{\text{wind}} \sum_{j \in G} k_j^{\text{BCID}} \left(1 - k_j^{\text{DT}}\right) \Delta t_j} \tag{6.6}$$

For a single luminosity block i (fully expanded using expressions 6.2 and 6.5) the flux is:

$$\Phi_\mu^i = \frac{1}{4 d_0^{\text{cut}} z_0^{\text{cut}} \epsilon_{\text{trig}} \epsilon_{\text{rec}} k^{\text{wind}}} \frac{N^{\text{BCID}}}{\left(N_i^{\text{empty}} - N_i^{\text{abort}}\right)} \frac{k_i^{\text{PS}} N_i^{\mu_{\text{meas}}}}{\left(1 - k_i^{\text{DT}}\right) \Delta t_i}. \tag{6.7}$$

6.4 Charge Ratio

The number of positively or negatively charged muons can be written as

$$N_{\mu}^{\pm} = \frac{1}{\epsilon_{\text{trig}}} \frac{1}{\epsilon_{\text{rec}}} \sum_{i \in G} k_i^{\text{PS}} N_i^{\mu^{\pm}_{\text{meas}}}, \tag{6.8}$$

where $N_i^{\mu^{\pm}_{\text{meas}}}$ is the number of positively (or negatively) charged muons recorded in luminosity block i. The cosmic muon charge ratio (see section 5.1.2) is then

$$k_{\mu}^{\pm} \equiv N_{\mu}^{+} / N_{\mu}^{-}, \tag{6.9}$$

where the final result is simplified by cancelling the common efficiency factors.

This definition makes several approximations. To perform an accurate calculation of this ratio a location within the detector would have to be chosen that would not bias the data towards one muon charge over the other. In this analysis no special technique was used to check for acceptance bias for one charge or the other [46]. The efficiencies for the muons were also approximated to be charge independent. A large value for the p_{T} cut helps produce a more accurate measurement of the cosmics muon charge ratio even though the acceptance region is approximated to be charge independent. All charged particles travelling through a magnetic field will have their trajectories curved where the amount of curvature depends on the particle's momentum and the direction of the curvature depends on the particle's charge. In a magnetic field lower p_{T} muons will travel along more curved trajectories while higher p_{T} muons travel along straighter paths. A high-p_{T} muon will follow a fairly straight trajectory and is less likely to be deviated in or out of the fiducial region by the magnetic fields thus reducing the bias of the acceptance region towards a muon of one charge or the other. The charge ratio calculated by this analysis is an approximation and is not directly comparable to other cosmic muon charge ratio measurements because no momentum correction will be made to account for the energy loss between Earth's surface and the ATLAS cavern nor for acceptance losses.

6.5 Parameter Inversion Technique

A completely different method for estimating the cosmic muon background to a physics analysis is the "parameter inversion technique". To estimate the number of

cosmic background events, a subset of the cuts are changed to better accept cosmic muons and reject muons from collisions. In a recent ATLAS dilepton resonance search the d_0 and z_0 cuts (where these position coordinates are with respect to the vertex) were adjusted to have larger maximum absolute values to accept more cosmic muons [45]. In addition to this, minimum absolute values of d_0 and z_0 were introduced to exclude the central region containing most of the collision data. After "inverting" the parameters the analysis codes are then rerun with the newly inverted parameters and the number of cosmic muon background events in the larger area is measured. A ratio of areas can then be used to estimate the cosmic muon background to the dilepton resonance search.

This technique has the benefit that the cosmic muon background is studied using the same data and cuts as are used for the physics analysis. By using the same data the cosmic muon background is measured over the exact same time period as the data used for the physics analysis. By using the same cuts and analysis procedure, the background estimate does not later have to be adjusted to match the cuts of the analysis. This techniques also avoids having to apply any corrections to estimate probability of cosmic muon being misidentified in a particular way, e.g. a cosmic muon in a dilepton resonance search has to be misidentified specifically as a pair of back-to-back muons. A drawback of the technique is that physics analyses generally use strict cuts to reduce the effects of backgrounds thus resulting in few events passing the selection cuts even when inverting a subset of the parameters to estimate the cosmic muon background.

Chapter 7

Results

7.1 General Properties of the Selected Runs

ATLAS has collected many millions of cosmic events since it recorded its first 7 TeV collisions; however, ATLAS was constructed to study LHC collision data and so when there are no beams in the accelerator the primary objective is not taking cosmic data but rather preparing the detector for the next set of collisions by performing calibrations and tests or making repairs. It is in fact quite rare that ATLAS takes dedicated cosmic runs that pass the run selection cuts specified for this analysis.

The number of runs that pass the selection cuts is small for various reasons. The experiment is often not in a stable state of cosmic data taking as one of the several different detector systems is down for calibrations or only a few luminosity blocks of data are taken before some settings are changed and jumps are seen in the level-1 acceptance rates and deadtime for the desired trigger. When this is not the case the collision trigger menus commonly used result in a very low data acquisition rate for high-p_{T} cosmic muons.

Data quality experts on ATLAS provide the collaboration with lists of good runs for analyses of collision data. This is not the case for cosmic data. The only run taken between early 2010 and early 2011 that passes the selection cuts defined in section 6.2.1 is described in Table 7.1. All the luminosity blocks in this table define the set G that is used in equation 6.6 of section 6.3 to calculate the cosmic muon flux.

The efficiency of the L1_MU6_EMPTY trigger is approximated to be the same as the efficiency of the L1_MU6 trigger used for collisions. This approximation is made because the trigger efficiency is not known for cosmics taken in dedicated cosmic runs

Table 7.1: Run Properties.

Run 152344 Friday April 02 2010 15:40:14 CEST Luminosity blocks 45-255	
Run Property	Value(s)
STACO Muon Reconstruction Efficiency (ϵ_{rec})	0.93 ± 0.02 (stat.) [44]
$L1\_MU6\_EMPTY$ Trigger Efficiency (ϵ_{trig})	0.82 ± 0.02 (stat.) [44]
Prescale for $L1\_MU6\_EMPTY$ (k^{PS})	14
BCIDs of the *empty* bunch group	7-871, 898-1765, 1792-3488
Number of BCIDs in the *empty* bunch group (N^{empty})	3430
Number of BCIDs in the *empty* bunch group that are also in the abort gap (N^{abort})	44
Total Number of BCIDs (N^{BCID})	3564
Time window fraction (k^{wind})	1 [47]

and because the cosmic muons being analysed are pseudo-projective. Similarly the reconstruction efficiency used is the same as for reconstructing muons measured in collision data because the cosmic muons are pseudo-projective.

The deadtime fraction of the L1_MU6_EMPTY trigger per luminosity block should be small for an accurate calculation of the cosmic muon flux. Selecting the correct balance of prescales for the different triggers helps to keep the deadtime fraction low. The average deadtime fraction for the L1_MU6_EMPTY trigger for a luminosity block in the set G is approximately 9.2%. The deadtime fractions and their distribution for the lumiblocks in the set G are shown in Figure 7.1. Note that the deadtime fraction, while only approximated by equation 3.1, is slightly skewed because it is calculated without cutting the BCIDs in the abort gap. A larger deadtime implies a larger cosmic muon flux. As is visible in Table 7.2, only a small fraction of firings of the L1_MU6_EMPTY trigger are in the abort gap region and so the overall effect on the deadtime fraction is relatively small.

The average duration of a luminosity block in the set G is approximately 121 s. It is not a constant for all LBs but depends on how long the CTP takes to fill the raw data files. The distribution of luminosity block durations is shown in Figure 7.2. The

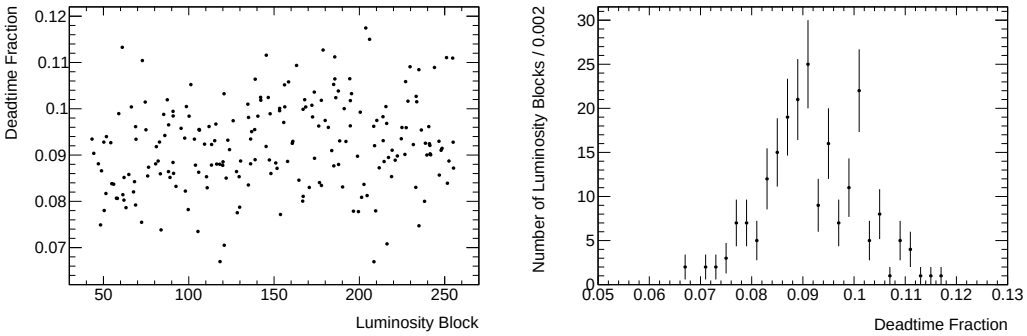

(a) Deadtime fraction for each LB (b) Deadtime fraction distribution

Figure 7.1: Deadtime fractions for the L1_MU6_EMPTY trigger.

total duration of all the lumiblocks in set G is 7 hours, 5 minutes, and 30.6 seconds.

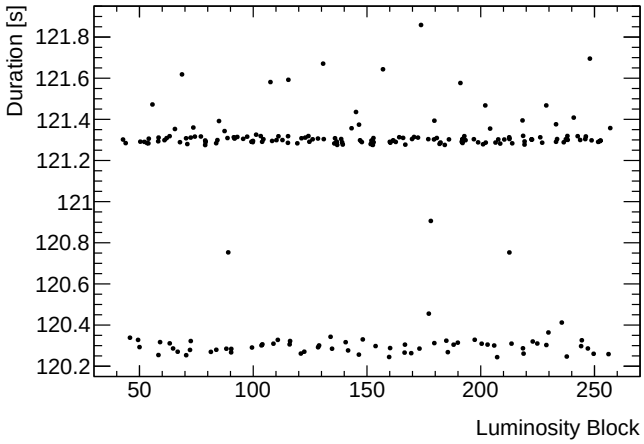

Figure 7.2: Luminosity block durations.

7.2 Particle Origin Checks

After the run selection and muon selection cuts, muon candidates are tested to ensure that the data analysed are really from cosmic rays. The distributions of the muon candidates' directions and transverse momenta can verify that they were from cosmic rays rather than other sources.

The distributions of the η and ϕ directions of the muon candidates, as seen in Figure 7.3, indicate that the muon candidates passing the cuts are consistent with cosmic rays. As discussed in section 6.3, most of the muon candidates are travelling

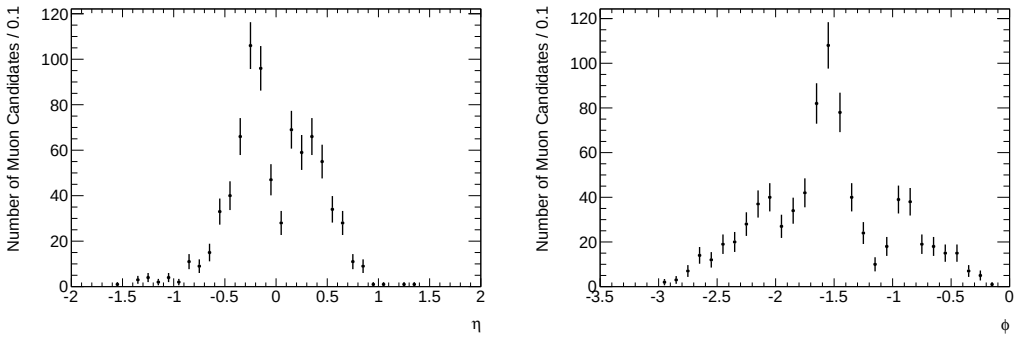

(a) η (b) ϕ

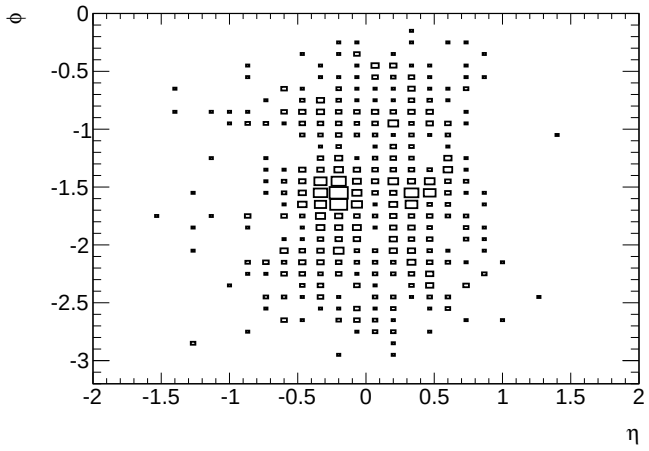

(c) ϕ - η

Figure 7.3: 1-D and 2-D histograms of the direction of the muon candidates as measured at the track perigee in η and ϕ.

close to vertically downward. The flux of muons underground decreases as the angle of the muons' trajectories from vertical increases because there is more material for the muons to traverse. This decrease in the cosmic muon flux is visible in the tails of the distributions of Figures 7.3a and 7.3b; the number of muons decreases to zero as $|\eta| > 1.5$ and as ϕ goes to 0 and $-\pi$ from $-\pi/2$ (which is vertically downward).

In Figure 7.3c the main two access shafts are visible as regions with a higher count of muons (although their separation is enhanced by the holes in detector coverage around $\eta \approx 0$ as discussed in section 2.3). The effect of the access shafts is more easily seen in Figure 7.3a.

Figure 7.3b shows a peak around $-\pi/2$ indicating that the majority of the muon candidates were travelling vertically downwards as projected into the $R-\phi$ plane. This

is partly the result of there being less material for the muons to traverse the closer to the vertically downwards direction the muons are travelling but is also emphasized by the access shafts being roughly centred over the detector in the ϕ direction. The actual distribution of muons *entering* the detector has only one wide central peak; however, a large number do not make it to the inner detector because they interact with the dead material of the toroid magnets and other instrumentation at $\phi \sim -3\pi/8, -5\pi/8$. As seen in Figure 7.3b, this results in a drop in the number of "combined" muons in these regions and it is this drop that creates the two peaks at $\phi \sim -0.9, -2.1$ (and not an increase in the flux of cosmic muons entering the detector at more horizontal angles).

The different sizes of the two peaks in the η distribution are due to the different sizes of the two access shafts. The acceptance region for the analysis defined by the d_0 and z_0 cuts is located roughly between the two shafts. The access shaft on the $+z$ axis side of the ATLAS cavern is the larger of the two main shafts, which results in a larger flux of muons travelling in the $-z$ (and therefore the $-\eta$) direction.

The distribution of the muon candidates' transverse momenta is shown in Figure 7.4. Figure 7.4b shows the higher-occupancy region of the distribution on a linear scale. The general shape of the distribution indicates that the number of muons drops off as a function of the transverse momentum. The curves start at 20 GeV, which is the minimum p_{T} cut imposed by the analysis. Figure 7.4a shows the distribution on a log-log scale. The complex geometry of the cavern makes it difficult to estimate the original distribution; however, ignoring the overburden entirely and using the most basic cosmic flux assumptions, the number of muon candidates passing the selection cuts should roughly follow an inverse power law as a function of energy and thus also as a function of the transverse momentum (see section 5.1.1). The function for this fit also neglects several effects including the geometry of the detector, the fact that muons can decay, other interactions that the cosmic particles undergo in the atmosphere, and the muon selection cuts. Part of the curve was fit using an inverse power law with two degrees of freedom: a scaling factor for the total number of muons and the exponent of the power law. The fit was done to check that the measured p_{T} distribution, despite all the effects distorting it, is still reasonably approximated by the inverse power law distribution described by the most simple model for the theory of cosmic muons.

Figure 7.5 shows the distribution of muon candidates as a function of BCIDs (after renumbering to count only the BCIDs that are in the *empty* bunch group and not

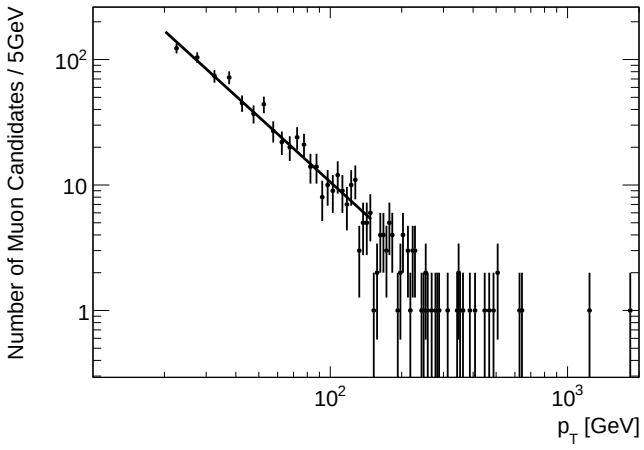

(a) p_{T} fit

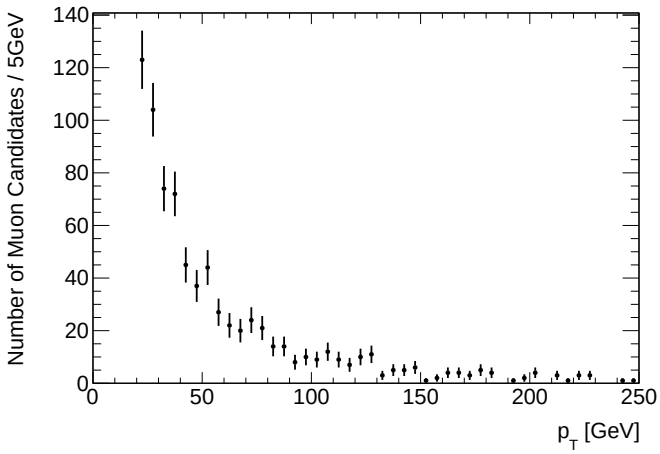

(b) p_{T}

Figure 7.4: p_{T} histograms with linear and logarithmic scales.

in the abort gap). The BCIDs that are not part of the *empty* bunch group and the BCIDs from the abort gap region are not included in the histogram because they have zero muons in them by design and would lower the height of the corresponding histogram bins. As expected, the results showed that no muon candidates that passed all the cuts were detected in these gaps.

The histogram of Figure 7.5 suggests that the flux is constant in time since the number of muon candidates detected in each renumbered BCID bin is approximately the same. The fit to the renumbered BCID distribution has a χ^2 per degree of freedom of 35.95/41 and a p-value of approximately 0.69 (note that the data in Figure 7.5 was binned in groups of large groups of BCIDs so the number of degrees of freedom was

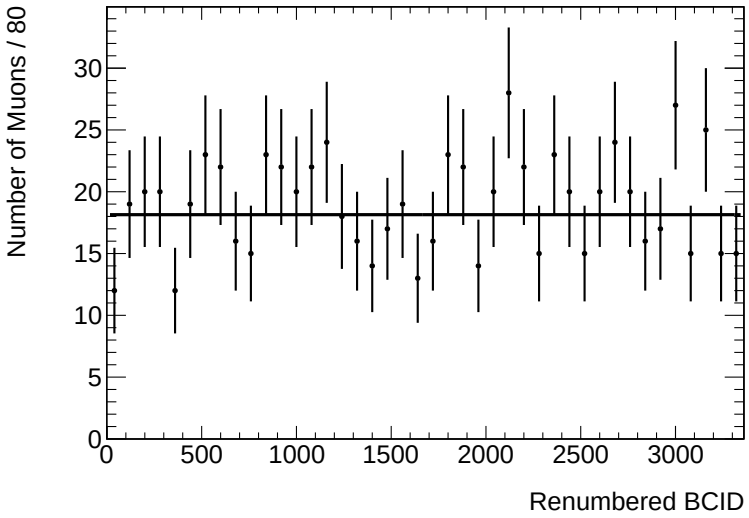

Figure 7.5: The renumbered BCID histogram shows the approximately constant distribution of muon candidates over the various BCIDs with the gaps removed.

greatly reduced).

7.3 Data Cuts

To calculate the cosmic muon flux reliably from data it is important to check the results after each of the selection cuts. The distributions of the detector hits and of the muon candidate perigee positions are used to ensure that the muons were reconstructed properly.

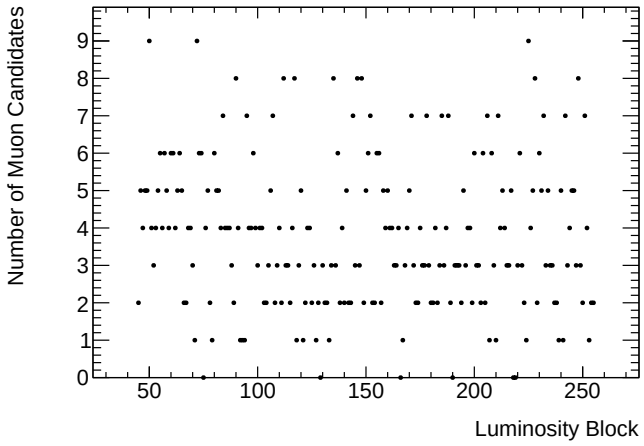

Figure 7.6: The number of muon candidates plotted for each luminosity block.

Table 7.2: Cut Flow.

Cut (see section 6.2.2)	Number of Events with ≥ 1 Cosmic Muon Candidates After Cut	Number of Cosmic Muon Candidates After Cut
Triggers	202529	264452
Abort Gap BCIDs	200637	262005
Combined Muon	5991	9829
SCT	3729	5905
MDT	3724	5872
z_0	2627	4050
d_0	1856	2694
p_{T}	802	802

Table 7.2 shows how the muon selection cuts filtered out data from the analysis and Figure 7.6 shows the number of muon candidates per luminosity block. The number of muon candidates that pass all the cuts is roughly three orders of magnitude less than the number of events where the trigger fired. Note that the number of events that pass the p_{T} cut and the number of cosmic muons candidates that pass the p_{T} cut are exactly the same because the analysis code allows for only one cosmic muon candidate per event. The code accepts the first cosmic muon candidate that passes all the cuts and throws out the rest from the event. In this analysis the p_{T} cut was the last cut and so it is after this cut that the number of events and the number of cosmic muon candidates match.

Figure 7.7 shows the number of hits along the muon candidate tracks for the different parts of the inner detector. A muon candidate track is reconstructed using hits from both the top and the bottom of the inner detector but only hits from either the top or the bottom half of the muon spectrometer as described in section 4.4.

The distributions depend strongly on the values of the d_0 and z_0 cuts. As is visible in Figure 7.7a there is a large spike at zero in the number pixel detector hits because the d_0 and z_0 cuts do not force the muons to traverse the pixel detector (see section 6.2.2). The d_0 and z_0 cuts do however require that (nearly) all the muons pass through all the layers of the SCT detectors and all detectors outside of the SCT. As can be seen in Figure 7.7b there is a peak around 16 SCT hits corresponding to roughly one hit in each SCT bi-layer in both the top and bottom halves of ATLAS in the barrel region. In Figure 7.7d a similar peak is seen at roughly 68 TRT hits which is close

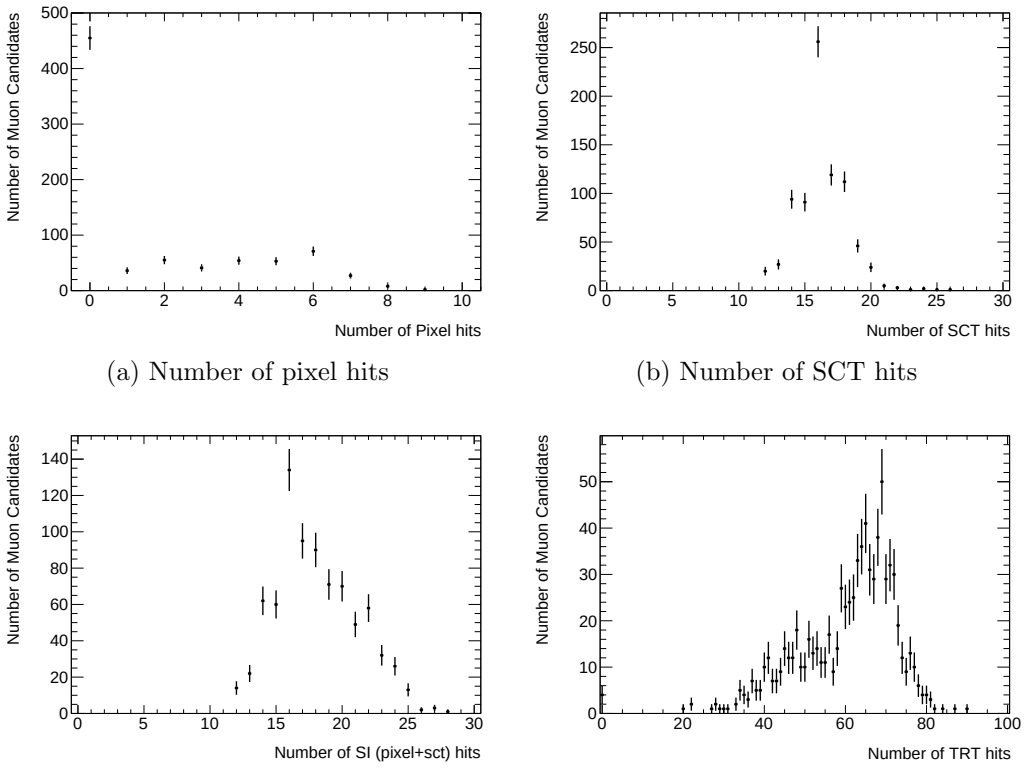

(a) Number of pixel hits

(b) Number of SCT hits

(c) Number of SI (pixel+SCT) hits

(d) Number of TRT hits

Figure 7.7: Number of hits along the muon candidate track in the different inner detector sub-detectors.

to twice number of TRT hits expected for a projective track. The number of hits for SCT and TRT sub-detectors has a peak with a width. The number of hits can be less than the peak value because the traversing muons may not ionize enough gas to register a hit, or something is preventing the sensor from producing a signal. In some cases the sensors are dead or have been masked because they are noisy. In other cases a sensor will also not be able to register a hit properly if it still has recently been hit by a different particle (this is the other form of deadtime). The number of hits per track in each sub-detector can be larger than the peak value because of the overlap of detector layers.

Figure 7.8 shows the number of hits along the muon candidate track in the different parts of the muon spectrometer. As expected, in Figure 7.8a there is a peak around 20 which corresponds to roughly the number of MDT tube layers in the muon spectrometer. The number of hits can be fewer than 20 if the muon simply did not cause a large enough ionization of gas in one or more MDTs, some of the tubes may

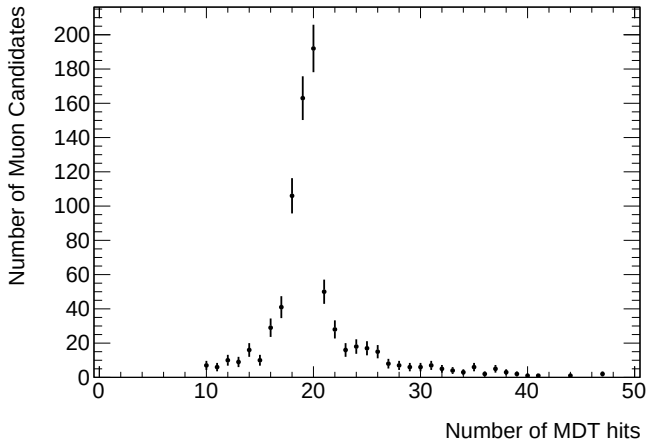

(a) Number of MDT hits

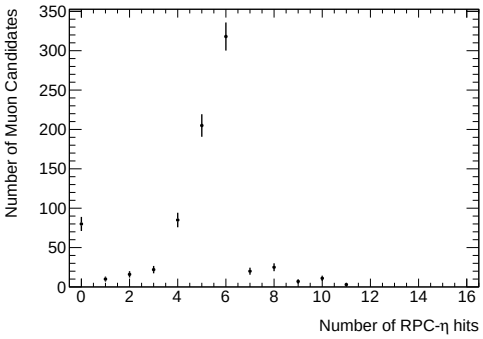

(b) Number of RPC η hits

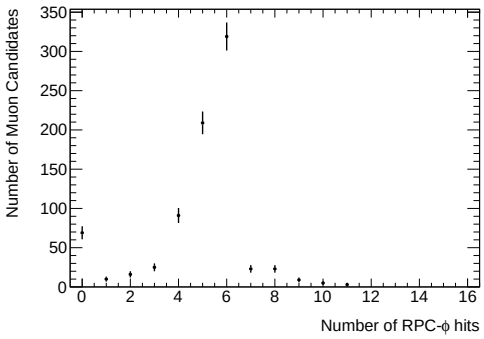

(c) Number of RPC ϕ hits

Figure 7.8: Number of hits along the muon candidate track in the different muon spectrometer sub-detectors.

be dead, masked because they are noisy or have just recently been hit by a different particle. The number of hits can be greater than 20 because in certain regions there is overlap between chambers. In general it is possible for a cosmic muon to traverse only the outer edges of the muon spectrometer; however, the d_0 cut, z_0 cut, and inner detector hits cuts require every muon to traverse all the layers of the muon spectrometer. Figures 7.8b and 7.8c show the hits for the RPCs for the η and ϕ coordinates. The distributions for the η and ϕ RPC hits look similar because the same RPC units are registering the hits for each coordinate measurement. Each distribution peaks around 6 hits which matches the total number of RPC layers. Again it is possible to register fewer than 6 RPCs hits for a muon if not enough ionization occurs, some of the sensors may be dead, masked because they are noisy or have just recently been hit by a different particle. It is possible for there to be more than 6 RPC hits because

of the overlap of muon chambers. While the triggering requires several detector layers to have fired in an event, these muon tracks can still register zero RPC hits because only half of the muon spectrometer is used to reconstruct the track or the track may have been triggered in the end-cap region by the TGCs.

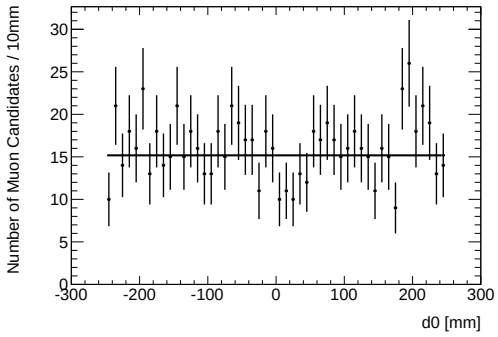

(a) d_0

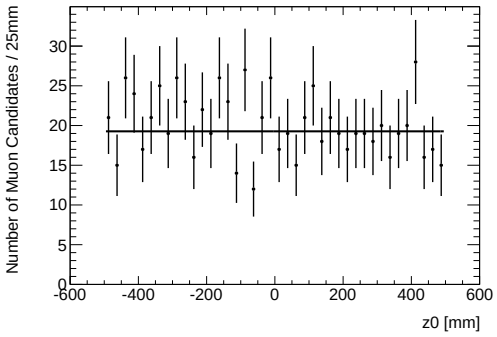

(b) z_0

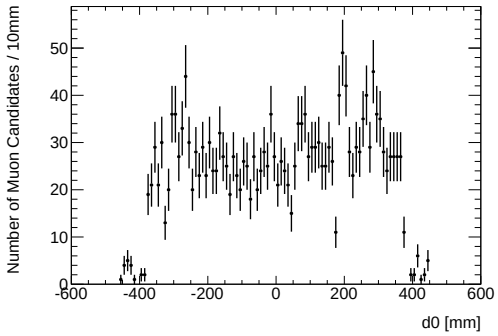

(c) d_0 without d_0 and z_0 cuts

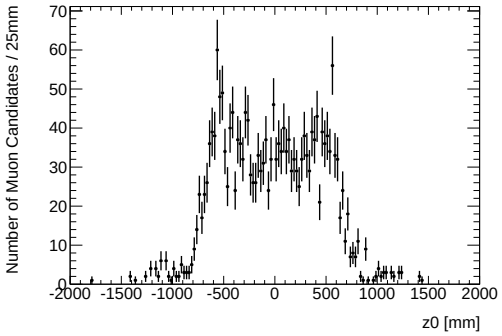

(d) z_0 without d_0 and z_0 cuts

Figure 7.9: d_0 and z_0 perigee coordinates histograms.

Figures 7.9a and 7.9b show the distribution of muon candidate perigee positions within the d_0^{cut}-z_0^{cut} cylinder. The d_0 and z_0 cuts are visible as the maximum and minimum values allowed for the coordinates. The flux of cosmic muon candidates is not constant over the entire detector's volume because of the variation in the amount of rock the muons traverse to get to different parts of the detector; however, over small areas the flux can be approximated as constant. The d_0 and z_0 cuts were partly chosen to ensure the reconstruction efficiency is constant for all the muon candidates passing the selection cuts (see section 4.4). To show the drop off in the reconstruction efficiency (see Figures 7.9c and 7.9d), the analysis was run again without imposing the d_0 and z_0 cuts. For the results of the cosmic flux calculation to be easily scaled for fluxes for smaller surface areas within this central part of ATLAS the cosmic flux

has to be constant throughout the surface area being studied in this analysis. The constants fit to each of the histograms in Figures 7.9a and 7.9b show this.

In the region of approximately 0 mm $< d_0 <$ 50 mm in the d_0 histogram there is a suggestive drop in the flux but if more muon candidates are added to the analysis by using additional triggers this dip disappears.

7.4 Cosmic Muon Flux

The cosmic muon flux can be calculated for the muon candidates in set G that passed the muon selection cuts by using equation 6.6 with the run properties given in Table 7.1, the perigee cuts from Table 6.1, the deadtime fractions shown in Figure 7.1a, and the luminosity block durations shown in Figure 7.2. The cosmic muon flux for muons with transverse momenta above 20 GeV is measured to be $1.34 \pm 0.06\,(\text{stat.})\ \text{s}^{-1}\ \text{m}^{-2}$. This value is of the same order of magnitude as the approximated flux of cosmic muons with energies above 20 GeV at sea level (or almost equivalently at the Earth's surface above the detector) of 6.0 $\text{s}^{-1}\ \text{m}^{-2}$ in the range $\theta < 75\,^\circ$ (see section 5.1).

The cosmic flux can also be calculated for each individual luminosity block using equation 6.7. As is visible in Figure 7.10 the flux is approximately constant in time. The fluxes in Figure 7.10 were calculated over periods of 8 luminosity blocks to get a significant sample in each period (see Figure 7.6). Fitting a constant to this a flux of $1.29 \pm 0.05\,(\text{stat.})\ \text{s}^{-1}\ \text{m}^{-2}$ is measured with the fit having a χ^2 per degree of freedom of 33.86/25.

7.4.1 Cosmic Muon Flux Assumptions, Approximations, and Systematic Uncertainties

Several assumptions and approximations were made in this analysis that contribute towards the systematic uncertainties. A number of systematic uncertainties exist in this experiment and analysis that need to be accounted for in any future deeper studies.

One of the larger sources of systematic uncertainty is the approximation of the flux through the fiducial region. The flux that is being claimed to have been measured in this analysis is that of the cosmic muons through the d_0^{cut}-z_0^{cut} plane; however, the muon candidates selected are those that traversed the surface of the d_0^{cut}-z_0^{cut}

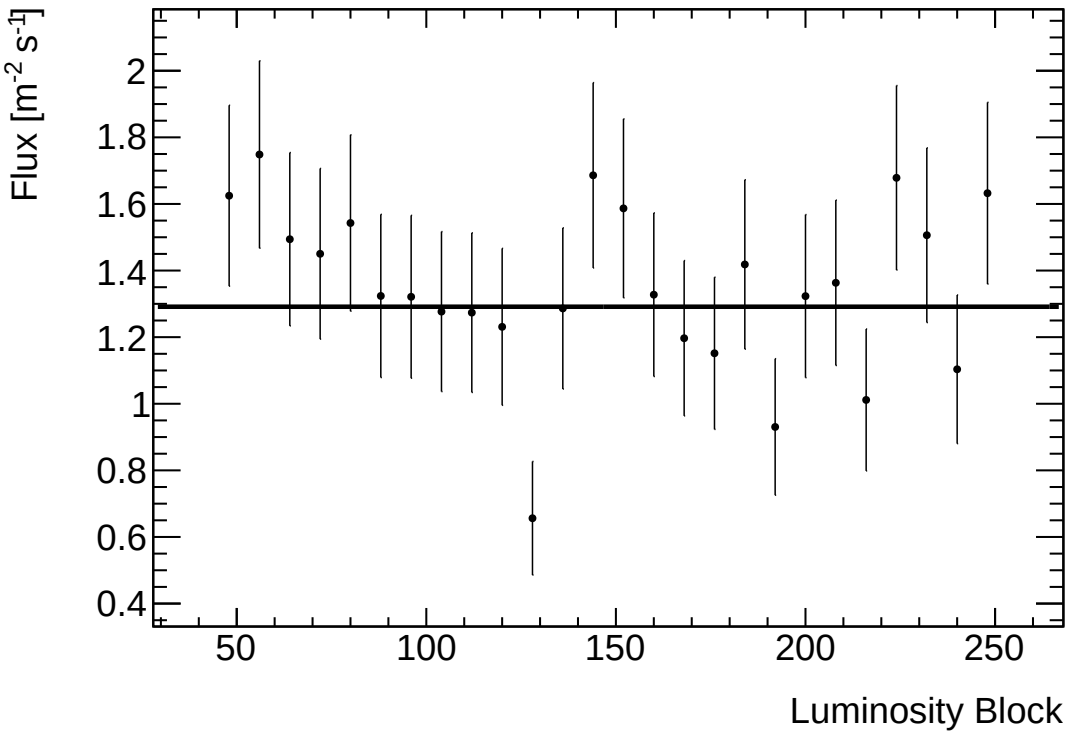

Figure 7.10: Cosmic muon flux measured over periods of 8 luminosity blocks to get a significant sample in each period.

cylinder (see section 6.2.2), which gives a flux that is slightly larger. The accuracy of this approximation is dependent upon the distribution of the muon trajectories: the closer to vertically downward the muons travel, the more accurate the approximation becomes. This approximation was tested by finding the intersection point of each track with the $y = 0$ plane assuming straight-line tracks. The fraction of cosmic muon candidates traversing the d_0^{cut}-z_0^{cut} plane was found to be 0.955 ± 0.007.

Many of the systematic uncertainties from the detector are combined together into the trigger efficiency and the reconstruction efficiency. These two efficiencies likely contribute some of the largest systematic uncertainties. One major systematic error has been introduced by approximating the triggering efficiency to be the same for cosmic muons as the trigger efficiency measured from collisions. The difference in the cosmic muons' trajectories and the collision muons' trajectories will cause the momenta to be measured slightly differently and the muons will traverse the detector coverage slightly differently. The trigger used in this analysis depends on the triggering detectors of the muon spectrometer (see section 3.2). A benefit of triggering on cosmic

muons is that since the particles traverse the full detector the muons can trigger in either the top or bottom of the detector, thus raising the trigger efficiency. Multiple scattering in the muon spectrometer can also introduce a systematic error as the muons may not stay within the desired trigger roads. A lower trigger efficiency is seen in regions of lower detector coverage such as the transition region between the barrel region, and the end-caps, and the regions of holes for cables, cryogenic cooling pipes, and the detector's feet (see Chapter 2). Some analyses introduce η-ϕ cuts to avoid these regions. Dead channels also lower the trigger efficiency in a similar way. The magnetic field of the muon spectrometer will also affect the track curvatures (see section 2.4) and any temporal variations in the magnetic field strength will also introduce systematic uncertainties.

The offline reconstruction of cosmic muons has additional systematic uncertainties associated with it because the whole detector is used to reconstruct the muons whereas the muon trigger just uses the muon spectrometer (see Chapter 4). As was the case with the trigger, dead channels, detector alignment, and multiple scattering all affect the reconstruction of the muons. Multiple scattering affects the measurement of p_{T} for high p_{T} muons. The calorimeters are especially likely to induce hard scatterings and potentially catastrophic energy losses (the loss of large amounts of energy), which reduce the reconstruction efficiency and the accuracy of the momentum measurements of combined muons. The reconstruction efficiency used for the cosmic muon candidates in this analysis was approximated to be the same as the reconstruction efficiency for muon candidates measured in collisions and this introduces several systematic uncertainties. The cosmic muons traverse the detector along slightly different paths because they do not originate near the interaction region. The lengths of the cosmic muon tracks can be beneficial because they introduce more detector hits and thus increase the probability of the track being reconstructed. The cosmic muons also traverse the full detector and the upper and lower halves of the detector will reconstruct the cosmic muons with slightly different efficiencies. The inherent resolutions of the position, energy, and momentum measurements are also subject to systematic uncertainties and affect the reconstruction efficiency but do not play a strong role in this analysis.

There is a also systematic uncertainty associated with the deadtime fractions (see equation 3.1). The deadtime is only approximated and has not been corrected for the triggered events removed from the BCIDs in the abort gap. For this analysis it was also assumed that there is no more than one cosmic muon per event because the flux

is small and only being studied over a small surface area. If this requirement were dropped then more muon candidates might be found and the measured value of the flux would increase. Another systematic error comes from approximating the flux to be constant in time (see section 5.1). The magnitude of the flux varies over long and short time scales. The number of muons from other sources that contaminate the data of this analysis is negligible because those muons would originate from very rare neutrino interactions.

7.5 Cosmic Muon Charge Ratio Calculation

The cosmic muon charge ratio can be calculated using equation 6.9 and the data from Tables 7.1 and 7.3. For muons with transverse momenta above 20 GeV the cosmic muon charge ratio is measured to be $1.3 \pm 0.1\,(\text{stat.})$. This was calculated without correcting for the dependence of the acceptance and efficiencies on the muon charges. The value is for the muons measured in the detector and not corrected to what it would be at the surface but it does still match the world average surface charge ratio value to within the uncertainty (see section 5.1.2).

Table 7.3: Charge Ratio Data.

Run 152344 Luminosity blocks 45-255	
Muon Count	Value
$\sum_{i \in G} N_i^{\mu^+_{\text{meas}}}$	460
$\sum_{i \in G} N_i^{\mu^-_{\text{meas}}}$	342
$\sum_{i \in G} k_i^{\text{PS}} N_i^{\mu^+_{\text{meas}}}$	6440
$\sum_{i \in G} k_i^{\text{PS}} N_i^{\mu^-_{\text{meas}}}$	4788

7.5.1 Cosmic Muon Charge Ratio Assumptions, Approximations, and Systematic Uncertainties

Many of the systematic uncertainties for calculating the cosmic muon charge ratio are the same as those for measuring the cosmic muon flux. Some of the systematic uncertainties cancel out with the division of the two muon counts (see equation 6.9) and others are not applicable like those related to time measurements. Several different systematic uncertainties are introduced in the charge ratio calculation because the muon charge is of importance. In this analysis the acceptance region was also assumed to be equally accessible to muons of both charges (see section 6.4). The reconstruction and triggering efficiencies were assumed to be the same for muons of both charges but these assumptions do not have a large effect [46].

Chapter 8

Conclusions

The ATLAS experiment at CERN is a multi-purpose particle physics detector. Many ATLAS analyses involve studying events with muons, including analyses studying top quarks and those searching for the elusive Higgs boson or particles from theories of physics beyond the Standard Model. The ATLAS detector is, however, constantly being bombarded by muons from cosmic rays, and events where pseudo-projective cosmic muons traverse the detector around the same time as a bunch crossing can be a background to physics studies.

The data analysed were taken in 2010 during a dedicated cosmic run where there were no beams in the LHC. While the ATLAS detector has measured many millions of cosmic muons, most of these were observed when proton beams were present in the LHC or when the detector was undergoing calibrations, or the data taking was performed using a trigger configuration not suited to this analysis. By understanding the different ways ATLAS triggers on, collects, reconstructs, and analyses data from cosmic rays and collisions, the deadtime fractions, trigger prescales, and efficiency factors were untangled to produce a measurement of the cosmic muon flux. The flux of cosmic muons with transverse momenta above 20 GeV in the central region of the detector has been measured to be $1.34 \pm 0.06\,(\text{stat.})\ \text{s}^{-1}\ \text{m}^{-2}$. This value is of the same order of magnitude as the estimated flux of cosmic muons above 20 GeV at the surface of $6.0\ \text{s}^{-1}\ \text{m}^{-2}$ covering the range $\theta < 75\,^{\circ}$. At the same time the cosmic muon charge ratio was measured to be $1.3 \pm 0.1\,(\text{stat.})$.

The analysis could be improved upon by calculating some of the systematic uncertainties as well as reducing them. Several efficiencies and data quality checks could be recalculated or recalibrated specifically for cosmic data taking rather than using approximations that these numbers should be the same as in the collision data tak-

ing scenarios. This measurement of the cosmic muon flux in ATLAS is the first step in one method of quantifying the sizes of the cosmic muon backgrounds to various physics analyses that look for events with high-p_{T} muons. This flux can be rescaled for different surface areas and an expected number of events contaminated by cosmic muons can be calculated specifically for each of the various physics analyses looking for events with high-p_{T} muons. The process for calculating the cosmic muon flux has been established and can be applied to more data from dedicated cosmic runs in the future.

More accurate measurements of the cosmic muon flux in ATLAS could be made in the future if some changes are made. To use the detector more effectively during cosmic data taking for a cosmic muon flux measurement, better documentation is required for the detector status and data quality, and the detector has to be in a steady state for longer continuous periods of time with appropriate trigger prescalings and deadtime fractions. Such changes would also allow this analysis to be expanded to look at cosmic muon data from collision runs. A good run list specifically for cosmic data and this cosmic muon flux analysis would be beneficial in that it might be possible to relax the prescale and deadtime fractions so that much more data could be analysed in a much quicker and more efficient manner. The methods given in this thesis can be used to direct further cosmic data taking for making more regular and accurate measurements of the cosmic muon flux over the lifetime of the experiment. These could help the experiment better understand the cosmic muon background to the ATLAS physics analyses.

Bibliography

[1] ATLAS Collaboration, G. Aad et al., *The ATLAS Experiment at the CERN Large Hadron Collider*, JINST **3** (2008) S08003.

[2] K. Nakamura et al., *Review of Particle Physics, 2010-2011. Review of Particle Properties*, Journal of Physics G **37** (2010) no. 7A, 075021. http://pdg.lbl.gov.

[3] M. L. Andrieux et al., *Construction and test of the first two sectors of the ATLAS barrel liquid argon presampler*, Nucl. Instrum. Methods Phys. Res., A **479** (2002) no. 2-3, 316–33.

[4] The ATLAS Collaboration, G. Aad et al., *Expected Performance of the ATLAS Experiment - Detector, Trigger and Physics*, Tech. Rep. arXiv:0901.0512. CERN-OPEN-2008-020, CERN, Geneva, 2009.

[5] *ATLAS Muon Spectrometer: Technical Design Report*. Technical Design Report ATLAS. CERN, Geneva, 1997. http://cdsweb.cern.ch/record/331068?ln=en. distribution.

[6] *ATLAS Magnetic System*, April, 2011. http://atlas-ma.web.cern.ch/atlas-ma/.

[7] *ATLAS central solenoid: Technical Design Report*. Technical Design Report ATLAS. CERN, Geneva, 1997. http://cdsweb.cern.ch/record/331067?ln=en.

[8] A. Yamamoto et al., *The ATLAS central solenoid*, Nucl. Instrum. Methods Phys. Res., A **584** (2007) no. 1, 53–74.

[9] *ATLAS Magnetic Field*, April, 2011. https://twiki.cern.ch/twiki/pub/Atlas/MagneticField/magplot.jpg.

[10] J. L. Baldy, J. Bremer, F. Butin, N. Delruelle, J. Gascon, F. Haug, J. Inigo-Golfin, R. Pengo, and I. Rühl, *ATLAS Infrastructure*, Tech. Rep. ATL-TECH-PUB-2008-002. ATL-COM-TECH-2008-002, CERN, Geneva, Mar, 2008.

[11] H. Rammer, *Novel Technique for the UX15 Cavern Vault Support System*, in *Proceedings of the Third ST Workshop*, no. CERN-ST-2000-021, pp. 301–305. Jan, 2000. st-div.web.cern.ch/st-div/workshop/ST2000WS/Proceedings/LHC1/hr.pdf.

[12] H. Rammer, *Two new caverns for LHC experiments: ATLAS and CMS*, CERN, 1998. http://cdsweb.cern.ch/record/357157. no. CERN-ST-98-005. As part of the the 1st Chamonix Workshop 1998, Chamonix, France.

[13] O. S. Brüning, P. Collier, P. Lebrun, S. Myers, R. Ostojic, J. Poole, and P. Proudlock, *LHC Design Report*. CERN, Geneva, 2004. http://cdsweb.cern.ch/record/782076/.

[14] H. Damerau and R. Garoby, *Creation and Storage of Long and Flat Bunches in the LHC*. PhD thesis, Tech. Univ. Darmstadt, Darmstadt, 2005. Presented on 01 Sep 2005.

[15] R. Bailey and P. Collier, *Standard Filling Schemes for Various LHC Operation Modes*, Tech. Rep. LHC-PROJECT-NOTE-323, CERN, Geneva, Sep, 2003.

[16] M. Stockton, *The ATLAS Level-1 Central Trigger*, Journal of Instrumentation **6** (2011) no. 01, C01075. Presentation given at Topical Workshop on Electronics for Particle Physics 2010, Aachen, Germany. Also under no. ATL-DAQ-PROC-2010-036.

[17] T. Pauly and the ATLAS Collaboration, *The ATLAS Level-1 Central Trigger System in Operation*, Journal of Physics: Conference Series **219** (2010) no. 2, 022017. http://cdsweb.cern.ch/record/1176568.

[18] S. Ask, D. Malon, T. Pauly, and M. Shapiro, *Report from the Luminosity Task Force*, Tech. Rep. ATL-GEN-PUB-2006-002. ATL-COM-GEN-2006-003. CERN-ATL-COM-GEN-2006-003, CERN, Geneva, Jul, 2006.

[19] *ATLAS level-1 trigger: Technical Design Report*. Technical Design Report ATLAS. CERN, Geneva, 1998. http://cdsweb.cern.ch/record/381429?ln=en.

[20] P. Jenni, M. Nessi, M. Nordberg, and K. Smith, *ATLAS High-Level Trigger, Data Acquisition and Controls: Technical Design Report*. Technical Design Report ATLAS. CERN, Geneva, 2003.

[21] S. Ask et al., *The ATLAS central level-1 trigger logic and TTC system*, Tech. Rep. ATL-COM-DAQ-2008-006, CERN, Geneva, Aug, 2008. JINST 3 (2008) P08002.

[22] M. Stockton, *The ATLAS Level-1 Central Trigger*, To be published in the proceedings for the Conference on Computing in High Energy and Nuclear Physics 2010, Taipei, Taiwan (CHEP2010) in Journal of Physics: Conference Series. See http://cdsweb.cern.ch/record/1322432, no. ATL-DAQ-PROC-2011-006.

[23] R. Spiwoks et al., *The ATLAS Level-1 Central Trigger Processor Core Module*, Tech. Rep. ATL-DAQ-2004-017, CERN, Geneva, 2004. IEEE/NSS 2004 Rome.

[24] R. Vari, July, 2011. Private communications with ATLAS RPC trigger expert.

[25] S. Hassani, L. Chevalier, E. Lanon, J.-F. Laporte, R. Nicolaidou, and A. Ouraou, *A muon identification and combined reconstruction procedure for the ATLAS detector at the LHC using the (MUONBOY, STACO, MuTag) reconstruction packages*, Nucl. Inst. & Meth. in Phys. Res. A **572** (2007) no. 1, 77–79. Frontier Detectors for Frontier Physics - Proceedings of the 10th Pisa Meeting on Advanced Detectors.

[26] *ATLAS Computing: Technical Design Report*. Technical Design Report ATLAS. CERN, Geneva, 2005. revised version submitted on 2005-06-20 16:33:46.

[27] R. Nicolaidou, L. Chevalier, S. Hassani, J. F. Laporte, E. Le Menedeu, and A. Ouraou, *Muon identification procedure for the ATLAS detector at the LHC using Muonboy reconstruction package and tests of its performance using cosmic rays and single beam data*, Journal of Physics: Conference Series **219** (2010) no. 3, 032052.

[28] G. Aad et al., *Measurement of the production cross section for W-bosons in association with jets in pp collisions at $\sqrt{s}$ = 7 TeV with the ATLAS detector.*, Tech. Rep. CERN-PH-EP-2010-081, CERN, Geneva, Dec, 2010. Submitted to Physics Letters B.

[29] A. E. Sandstroem, *Cosmic Ray Physics*. North-Holland Publishing Company, Amsterdam, 1965.

[30] P. K. F. Grieder, *COSMIC RAYS AT EARTH Researcher's Reference Manual and Data Book*. Elsevier Science Ltd., Amsterdam, 2001. http://www.sciencedirect.com/science/book/9780444507105.

[31] M. G. K. Menon and P. V. R. Murthy, *Cosmic Ray Intensities Deep Underground*, Progress in Elementary Particle and Cosmic Ray Physics .

[32] *High energy cosmic rays striking atoms at the top of the atmosphere give the rise to showers of particles striking the Earth's surface*, April, 2011. CERN, http://cdsweb.cern.ch/record/40407.

[33] O. C. Allkofer, *Introduction to Cosmic Radiation*. K. Thiemig, 1975.

[34] T. K. Gaisser, *Cosmic rays and Particle Physics*. Cambridge and New York, Cambridge University Press, 1990, 292 p., 1990.

[35] T. Hebbeker and C. Timmermans, *A compilation of high energy atmospheric muon data at sea level*, Astroparticle Physics .

[36] W. R. Frazer, C. H. Poon, D. Silverman, and H. J. Yesian, *Limiting Fragmentation and the Charge Ratio of Cosmic-Ray Muons*, Phys. Rev. D **5** (1972) no. 7, 1653–1657.

[37] *Luminosity Public Results*, June, 2011. https://twiki.cern.ch/twiki/bin/view/AtlasPublic/LuminosityPublicResults#Data_Taking_Efficiency_and_Pileu.

[38] M. Klute, *A study of the weak boson fusion, with $H \to \tau^+\tau^-$ and $\tau \to e\,(\mu)\,\nu_{e,(\mu)}\nu_\tau$*, Tech. Rep. ATL-PHYS-2002-018, CERN, Geneva, Mar, 2002. revised version number 1 submitted on 2002-09-02 21:13:38.

[39] F. del Aguila, *The Physics of Z' bosons*, Acta Phys. Polon. **B25** (1994) 1317–1336.

[40] *Search for high mass dilepton resonances in pp collisions at* $\sqrt{s} = 7$ TeV *with the ATLAS experiment*, Tech. Rep. ATLAS-CONF-2011-083, CERN, Geneva, Jun, 2011.

[41] *Search for high-mass states with one muon plus missing transverse momentum in proton-proton collisions at* $\sqrt{s} = 7$ TeV *with the ATLAS detector*, Tech. Rep. ATLAS-CONF-2011-082, CERN, Geneva, Jun, 2011.

[42] R. Brun and F. Rademakers, *ROOT - An object oriented data analysis framework*, Nucl. Inst. & Meth. in Phys. Res. A **389** (1997) no. 1-2, 81 – 86. Proceedings AIHENP'96 Workshop, Lausanne, Sep, 1996. See also http://root.cern.ch/.

[43] G. Aad et al., *Search for high-mass states with one lepton plus missing transverse momentum in proton-proton collisions at* $\sqrt{s} = 7$ *TeV with the ATLAS detector.*, Tech. Rep. arXiv:1103.1391. CERN-PH-EP-2011-023, CERN, Geneva, Mar, 2011. Accepted by Physics Letters B.

[44] ATLAS Collaboration, G. Aad et al., *Measurement of the* $W \to \ell\nu$ *and* $Z/\gamma* \to \ell\ell$ *production cross sections in proton-proton collisions at* $\sqrt(s) = 7$ TeV *with the ATLAS detector*, Journal of High Energy Physics **2010** (2010) 1–65.

[45] ATLAS collaboration, *Performance of the ATLAS Muon Trigger in p-p collisions at* $\sqrt{s} = 7$ TeV, Tech. Rep. ATLAS-CONF-2010-095, CERN, Geneva, Oct, 2010. http://cdsweb.cern.ch/record/1299573.

[46] A. Belloni, K. Black, J. P. B. Guimaraes da Costa, J. Huth, L. Kashif, T. Lazovich, J. Kearney, V. I. Martinez Outschoorn, S. Prasad, W. Spearman, and M. Swiatlowski, *Measurement of the Cosmic Ray Muon Charge Ratio using the ATLAS Muon Spectrometer*, Tech. Rep. ATL-COM-MUON-2010-012, CERN, Geneva, Jun, 2010. ATLAS internal report.

[47] M. D. Volpe, M. Iodice, and R. Vari, June, 2011. Private communications with ATLAS Muon and RPC experts.

Appendix A

Abbreviations, Acronyms and Symbols

A.1 List of Symbols

c	speed of light in a vacuum
p_{T}	transverse momentum
E_{T}	transverse energy
d_0^{cut}	cut along z direction
z_0^{cut}	cut along the radial direction
A	Area for flux calculation
N_μ	Number of muons after all scalings (scaling example: prescales)
$N_i^{\mu_{\mathrm{meas}}}$	Number of muons passing the cuts (no scaling) in luminosity block i
Δt	Elapsed time after all scalings (scaling example: deadtime fraction)
Δt_i	Duration of luminosity block i (no scaling)
G	The set of all good luminosity blocks used for the analysis
ϵ_{trig}	Trigger efficiency
ϵ_{rec}	Reconstruction efficiency
k_i^{PS}	Trigger prescale in luminosity block i
k^{wind}	"Time window fraction" - Fraction of time that the detector is capable of recording data per BCID

k_i^{BCID}	Fraction of BCIDs used in the analysis in luminosity block i
N_i^{empty}	Number of BCIDs in the *empty* bunch group in luminosity block i
N_i^{abort}	Number of BCIDs in the abort gap overlapping the *empty* bunch group in luminosity block i
N^{BCID}	Total Number of BCIDs
k_i^{DT}	Deadtime fraction for luminosity block i

A.2 List of Abbreviations and Acronyms

BCID	Bunch-Crossing Identification or Bunch-Crossing Identifier (ambiguous)
CERN	Organisation Européenne pour la Recherche Nucléaire (The European Organization for Nuclear Research) - Acronym from the original name "Conseil Européen pour la Recherche Nucléaire"
CSC	Cathode Strip Chamber
CTP	Central Trigger Processor
EF	Event Filter
EM	Electromagnetic
HLT	High Level Trigger
LAr	Liquid Argon
LEP	Large Electron Positron (collider)
LHC	Large Hadron Collider
Lumiblock	Luminosity block
L1	Level-1 (trigger)
L1A	Level-1 Accept Signal
L2	Level-2 (trigger)
MDT	Monitored Drift Tube
PS	Prescale
RF	Radio Frequency
RPC	Resistive Plate Chamber
SCT	SemiConductor Tracker
TGC	Thin Gap Chamber
TRT	Transition Radiation Tracker

Appendix B

Terms

Athena	The code framework for processing and analyzing of ATLAS data
ATLAS	The name of the collaboration and the particle physics experiment
BCID	A label for the crossings of the different possible bunch positions
CERN	One of the world's largest scientific organizations
Calorimeters	Energy measurement devices
Cosmic muon charge ratio	The ratio of the number of positively charge cosmic muons to the number of negatively charged cosmic muons
CSC	Muon chambers in the end-caps, used for both triggering and precision reconstruction.
Doublet	A set of two detector layers physically built as one unit
EF	The last trigger level that filters the data (Even Filter)
HLT	Collective name for the L2 trigger and the event filter
Inner detector	Inner tracking detector
Interaction region	The volume where beam interactions occur at the centre of ATLAS
LHC	The particle accelerator that collides the beams producing the particles that ATLAS observes
Luminosity	A measure of the rate at which particles collide (related to the intensity of the beams)

Luminosity block	A short time interval of data taking
L1 trigger	The first trigger that the filters data
L2 trigger	The second trigger that the filters data
MDT	Muon chambers used for precision reconstruction, in both barrel and end-caps.
Perigee	The point of closest approach of a track to the centre of ATLAS
Pixel Tracker	Innermost layer of the inner detector. Is used for high resolution tracking
Possible bunch position	An RF bucket labelled as allowed to hold a proton bunch
Proton bunch	A grouping of about 10^{10} protons accelerated and collided with other bunches by the LHC
RF bucket	A trap for a proton bunch generated by the RF system
RPC	Muon chamber used for the Level-1 Muon Trigger in the barrel region.
Solenoid magnet	Produces the magnetic field for the inner detector
SCT	Middle layer of the inner detector. Is used for high resolution tracking
Tile Calorimeter	The hadronic calorimeter in the barrel region
TGC	Muon chamber used for the Level-1 Muon Trigger and precision muon tracking in the end-cap regions.
Toroid magnet	Produces the magnetic field for the muon spectrometer
Track	The path of a charged particle
Triplet	A set of three detector layers physically built as one unit
TRT	Outermost sub-detector of the inner detector. Is used to measure a large number of track hits
Vertex	An interaction point where the accelerated particles collide and from which the detected particles emanate.